

**Rheinisch-Westfälische Technische Hochschule Aachen**

**Lehrstuhl für Werkstoffchemie**

**Master's Thesis**

**by**

**Raghu Praveen Pubbysetty**

born on 27.12.1991 in YSR Kadapa, India

Matriculation number: 340951

**Developing the CMAS (CaO-MgO-Al<sub>2</sub>O<sub>3</sub>-SiO<sub>2</sub>) resistant TBCs  
(Thermal Barrier Coatings): Alumina (Al<sub>2</sub>O<sub>3</sub>) as a candidate for  
restricting the CMAS infiltration in TBCs.**

Carried out at German Aerospace Centre, Köln

Aachen, July 2016

**First Examiner: Prof. Jochen M. Schneider, Ph. D**

**External Supervisor: Dr. Ravisankar Naraparaju**

## **Statutory Declaration**

The present thesis was carried out at DLR, Köln in collaboration with Department of Materials Chemistry (MCh), RWTH Aachen University.

I hereby declare that I have written this thesis independently, that I have not made use of sources and means other than those listed, and that I have indicated all citations.

---

Date

---

Signature

Inhalt und Ergebnisse dieser Arbeit sind ausschließlich zum internen Gebrauch bestimmt. Alle Urheberrechte liegen bei der RWTH Aachen. Ohne ausdrückliche Genehmigung des betreuenden Lehrstuhls ist es nicht gestattet, diese Arbeit oder Teile daraus an Dritte weiterzugeben.

(Content and results of this work are intended solely for internal use. All copyrights belong to the RWTH Aachen University. Without the express permission of the supervising Chair, it is not permitted to pass on this work or parts of it to third parties.)

## **Dedication**

I dedicate this work to my parents whose unconditional support and encouragement have always helped me to keep going and grow as an individual and professional.

## **Acknowledgements**

I want to express my most sincere gratitude to all the individuals who have contributed to the completion of this thesis project. First, to my advisor Prof. Jochen M Schneider who gave me the opportunity to work in this fascinating project and provided guidance and support during all this learning process. Second, to my project supervisor Dr. Ravisankar Naraparaju who also was a key individual in making this project possible and guided me during my 6-month research term at DLR. I would like to thank Prof. Dr. Uwe Schulz and Dr. Peter Mechnich for their shared expertise and critical input to this project.

## Abstract

The rise in aero-engine operating temperatures due to economic and environmental issues has generated many technological inventions. Few among them are the development of new generation super alloys which can tolerate higher temperatures and high stresses, and the evolution of ceramic coatings on top of the alloys which can reduce the temperature load. These thermal barrier coatings (TBCs) are mainly deposited by electron beam physical vapor deposition (EB-PVD), which has inter-columnar porosity, and by air plasma spraying (APS), which has porosity and cracks mainly running parallel to the interface. These TBCs are used in protecting combustion chamber walls, turbine blades and vanes allowing higher operating temperatures of aero-engines. CMAS ( $\text{CaO-MgO-Al}_2\text{O}_3\text{-SiO}_2$ ) attack becomes more dominant in the increased temperature range of current aero-engines. Currently 7 wt. % Ytria Stabilized Zirconia (7YSZ) has been used as a TBC in aero-engines. As CMAS melts at temperature  $1200^\circ\text{C}$  and above, it infiltrates through the porous inter-columnar TBC structure with help of capillary forces. This infiltration causes severe mechanical stresses within the TBC upon thermal cycling subsequently leading to crack formation and TBC spallation. As the state of the art 7YSZ TBC coatings could not resist the CMAS infiltration, the development of an EB-PVD alumina layer as an alternative CMAS resistant coating will be part of this work. The fabrication of EB-PVD  $\text{Al}_2\text{O}_3$  on top of 7YSZ coatings was achieved by varying the deposition process parameters and the corresponding morphology of EB-PVD  $\text{Al}_2\text{O}_3$ /7YSZ coatings was studied. The coatings were deposited on alumina substrates in order to conduct long term infiltration tests. CMAS infiltration experiments were performed at  $1225^\circ\text{C}$  and  $1250^\circ\text{C}$  for different time intervals starting from 1 to 10 hours. In addition, very short term infiltration tests for 5 minutes were performed at  $1250^\circ\text{C}$  using a model CMAS source and a real volcanic ash. The results show that the studied EB-PVD  $\text{Al}_2\text{O}_3$ /7YSZ coatings induced the crystallization of the CMAS melt by forming stable spinel ( $\text{MgAl}_{1.9}\text{Fe}_{0.1}\text{O}_4$ ) and anorthite ( $\text{CaAl}_2\text{Si}_2\text{O}_4$ ) phases which were characterized by scanning electron microscopy and energy dispersive spectroscopy. These layers exhibit a minimal growth making EB-PVD alumina topcoat a promising candidate for CMAS resistant multilayer TBCs. However, the EB-PVD  $\text{Al}_2\text{O}_3$  samples experienced heavy sintering during long time exposure at high temperatures and the formed cracks in the layer have allowed the CMAS to fully infiltrate. Thus, multifunctional reaction-bonded alumina oxide (RBAO) was deposited on top of EB-PVD  $\text{Al}_2\text{O}_3$  which acts as a sacrificial layer forming the stable CMAS arresting products and inhibiting further infiltration.

## List of Symbols and Abbreviations

### Symbols

<b>Symbol</b>	<b>Description</b>
T	Temperature in °C
T <sub>m</sub>	Melting temperature
t	Time
p	Pressure in mbar
Wt. %	Weight Percent
rpm	Rotations per minute
θ	Bragg angle

### Abbreviations

<b>Acronym</b>	<b>Description</b>
TBC	Thermal Barrier Coating
EB-PVD	Electron Beam Physical Vapor Deposition
CVD	Chemical Vapor Deposition
PLD	Pulsed Laser Deposition
APS	Air Plasma Sprayed
7YSZ	7 wt. % Yttria Stabilized Zirconia
TGO	Thermally Grown Oxide
CMAS	Calcium Magnesium Alumina Silicate
VA	Volcanic Ash
SEM	Scanning Electron Microscopy
XRD	X-ray Diffraction
EDX	Energy Dispersive X-ray analysis
HP	High pressure
LP	Low Pressure
RBAO	Reaction-bonded alumina oxide

## Table of Contents

Statutory Declaration .....	ii
Acknowledgements.....	iv
Abstract.....	v
List of Symbols and Abbreviations.....	vi
Abbreviations.....	vi
Chapter 1: Introduction and Problem Definition .....	1
1.1 Problem Statement .....	2
1.2 Significance.....	3
1.3 Objectives.....	3
Chapter 2: Literature Review.....	4
2.1 Thermal Barrier Coating System (TBCs).....	4
2.2 Electron Beam Physical Vapor Deposition (EB-PVD).....	6
2.3 Ceramic Topcoat .....	8
2.3.1 7YSZ.....	8
2.3.2 Thermally Grown Oxide (TGO).....	10
2.3.3 Bond Coat .....	10
2.3.4 Superalloys .....	11
2.3.5 Alumina (Al <sub>2</sub> O <sub>3</sub> ).....	11
2.4 Calcium Magnesium Alumina Silicate (CMAS) .....	13
2.4.1 Thermochemical Attack .....	14
2.4.2 Thermomechanical Attack.....	14
2.5 Efforts in restricting CMAS induced damage in TBCs.....	15
2.5.1 EB-PVD Alumina top coat as a CMAS restricting TBC.....	15
2.6 Sintering Effect .....	16
2.7 Reaction Bonded Alumina oxide (RBAO) .....	16
Chapter 3: Experimental Procedure .....	17
3.1 EB-PVD Al <sub>2</sub> O <sub>3</sub> /7YSZ TBC preparation .....	17
3.2 CMAS and Volcanic ash compositions.....	18
3.3 X-Ray Diffraction Analysis .....	19
3.4 Infiltration Tests .....	20

3.4.1 Short Term CMAS Infiltration tests for Alumina/7YSZ Coatings.....	20
3.4.2 Long Term CMAS Infiltration tests for Alumina/7YSZ Coatings.....	21
3.5 Manufacturing of RBAO on EB-PVD Alumina/7YSZ TBC.....	22
3.6 Characterization of CMAS Infiltrated Samples .....	23
Chapter 4: Experimental Results .....	24
4.1 Fabrication of EB-PVD Al <sub>2</sub> O <sub>3</sub> on top of 7YSZ TBCs .....	24
4.1.1 Manufacturing the EB-PVD alumina top layer on 7YSZ.....	24
4.1.2 Alumina Phase characterization and transition using In-situ XRD.....	26
4.1.3 Sintering effect on the morphology of EB-PVD Al <sub>2</sub> O <sub>3</sub> /7YSZ TBCs.....	27
4.1.4 Phase characterization of CMAS and volcanic ash alumina powders.....	28
4.2 CMAS/VA Infiltration tests .....	29
4.2.1 Short Term Infiltration Tests at 1250°C.....	29
4.2.2 Long Term Infiltration Tests at 1250°C .....	33
4.2.3 Long Term Infiltration Tests at 1225°C .....	40
4.3 CMAS Infiltration Tests on RBAO Alumina/7YSZ .....	47
4.3.1 Infiltration Analysis on RBAO topcoat after 10h at 1250°C.....	47
Chapter 5: Discussion .....	51
5.1 Manufacturing the EB-PVD alumina top layer on 7YSZ .....	51
5.2 CMAS/VA Infiltration Tests.....	52
5.2.1 Reaction Layer Analysis for CMAS 1.....	52
5.2.2 Reaction Layer Analysis for Krämer CMAS .....	53
5.2.3 Reaction Layer Analysis for Iceland VA .....	54
5.2.4 Reaction layer Growth and Temperature Dependency.....	55
5.3 Infiltration Analysis on RBAO Alumina top coat.....	57
Chapter 6: Conclusion.....	59
Bibliography .....	61

## Chapter 1: Introduction and Problem Definition

Modern aero-gas turbines operating in energy, transportation and defense zones particularly rely on high-temperature thermal barrier coatings (TBCs) for improved efficiencies and power. Worldwide TBC research expresses continuous efforts to increase the lifetime efficiency. Particularly focusing on turbine blades and vanes (see Fig.1.1) from a materials perspective, they must withstand not only the mechanical properties, but also the high temperature exposure, oxidation and corrosion attack.

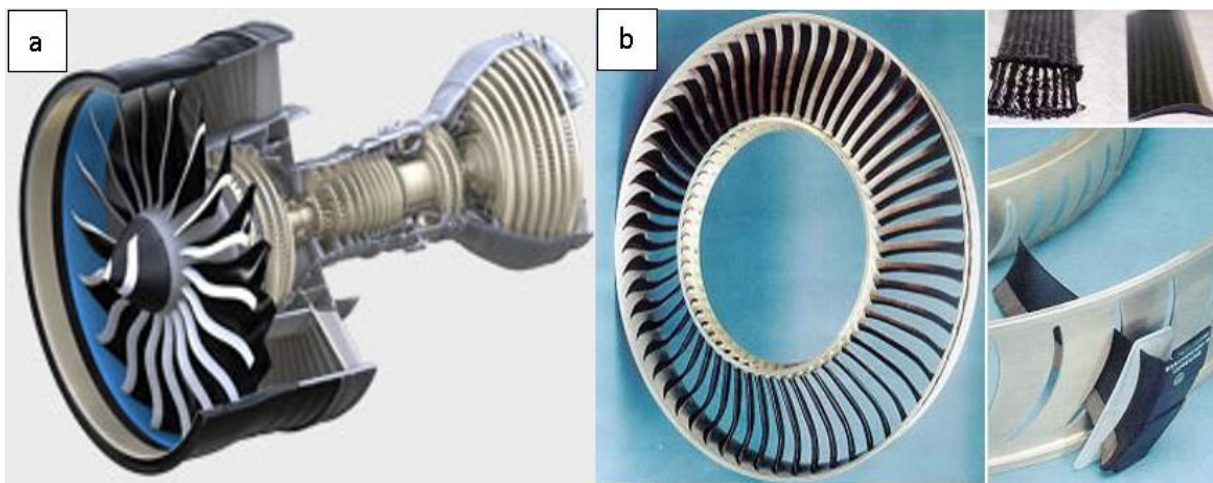


**Figure 1.1:** (a) The GE9X is the most fuel efficient, low-emissions jet engine that GEAE developed for Boeing 787 and 747-8 aircrafts, (b) Honeywell Jet Engine Stator Vane [1].

The temperatures generated in the combustion chamber of aero-gas turbine engines are drastically high enough to damage turbine blades. Advanced cooling techniques utilize a combination of internal (forced convection, impingement cooling) and external (film cooling) systems, with the addition of TBCs, to increase efficiency and life time of different gas turbine engine parts [2, 3]. TBCs are most commonly used as insulation material and to improve the durability of engine parts which also leads to an increase in the engine operating efficiency [4]. These TBCs are mainly deposited by electron beam physical vapor deposition (EB-PVD) or by air plasma spraying (APS). The EB-PVD top coats have inter-columnar porosity whereas the APS have porosity and cracks mainly running parallel to the interface. The differences in TBCs of EB-PVD and APS are mainly because of shape, orientation and distribution of their porosity [2, 5]. The columnar gaps formed on the coatings grown by EB-PVD technique offer a higher strain tolerance and thermal shock resistance upon thermal cycling, but they lead to a higher thermal conductivity than TBCs grown by the APS technique [6]. Normally APS coatings were

used on stationary engine parts like the combustor and shroud, whereas EB-PVD coatings were mainly used on challenging high temperature zonal parts like blades and vanes [1].

Typically, TBCs were made up of ~7 wt. %  $Y_2O_3$  stabilized  $ZrO_2$  (7YSZ) ceramics. Its combination of porosity and very low thermal conductivity provides the properties for an excellent high temperature insulator. Furthermore, TBCs must be mechanically tough to erosion and able to sustain fractures. Siliceous minerals such as sand, dust, volcanic ash, and runway debris are ingested into the combustion chamber through intake of air. These CMAS ( $CaO-MgO-Al_2O_3-SiO_2$ ) particles pass on into turbine combustion chambers where they melt and start infiltrating to the bottom of the TBCs, thereby affecting not only the TBC layers but also the substrate alloy. Due to this, CMAS resistant layer of TBCs must be developed [7].

### 1.1 Problem Statement

The increase in operating temperatures of modern aero-engines due to economic and environmental issues led to the evolution of TBCs which can lower the temperature load. The CMAS/Volcanic ash attack becomes more dominating in increased temperature range of aero-gas turbine engines. The hot corrosion attack of these siliceous particles with respect to TBCs leads to eventual failure of TBCs. Hence, there is a critical demand for TBC systems that enable higher operating temperatures with high reliability. The goal of this project is to develop a CMAS resistant EB-PVD alumina top coat. A new multilayer TBC structure can be developed keeping the standard 7YSZ as a base layer for thermal insulation and EB-PVD alumina as a CMAS resistant top coat as shown in Fig. 1.2.

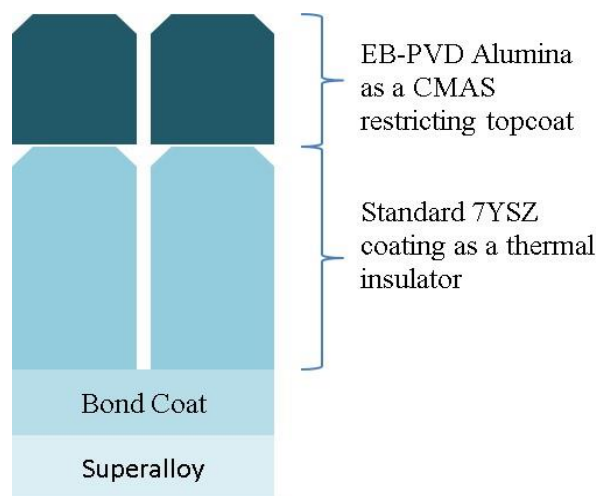


**Figure 1.2:** Proposed multilayered CMAS restricting EB-PVD alumina topcoat.

## 1.2 Significance

The siliceous minerals ( $\text{CaO-MgO-Al}_2\text{O}_3\text{-SiO}_2$  (CMAS)), which are widely spread in the atmosphere and commonly identified in sand, runway debris, and volcanic ash, have a substantial effect on aircraft engines. Therefore, a higher pressure has been put on aircraft engine manufacturers to effectively address this CMAS/VA attack issue and reduce economical losses for future events. EB-PVD alumina shows a potential for CMAS arrest in TBC systems. However, there is no available literature on fabricating a columnar EB-PVD alumina top coat or infiltration tests using CMAS/VA on EB-PVD alumina coatings. Thus, a better understanding of CMAS/VA with EB-PVD alumina interaction at high temperature can lead to significant benefits in the performance and lifetime extension for aero-gas turbine engines.

## 1.3 Objectives

Ceramic deposited by EB-PVD exhibit a cyclic thermal spallation lifetime 8-15 factor higher than the APS coatings [8]. However, the phase content and morphology of EB-PVD alumina entirely depends on process parameters, primarily substrate temperature, chamber pressure, and deposition rate. It was known from the literature that during the in-situ alumina deposition there was an unstable melt pool and melt spitting [9]. So fabricating EB-PVD alumina is an ultimate challenge. As the state of art 7YSZ TBC coating could not resist the CMAS/VA infiltration, the development of EB-PVD alumina layer as an alternative CMAS resistant coating will be part of my work.

- ❖ A key goal is to develop CMAS resistant TBCs.
- ❖ The main goal is to deposit EB-PVD alumina on top of 7YSZ.
- ❖ Main focus is to evaluate the reaction of alumina with CMAS/VA.
- ❖ Understanding the infiltration behavior of CMAS in EB-PVD alumina layers.

## Chapter 2: Literature Review

### 2.1 Thermal Barrier Coating System (TBCs)

TBCs are refractory-oxide ceramic coatings which are applied to the surface of metallic parts in the combustion chamber, turbine blades, and vanes of aero gas turbine engines, stationary turbines, etc., [10]. These TBCs are specifically used in the high temperature regions of gas-turbine engines, as shown below in Fig. 2.1 [1]. As the working temperature at the hot-section components of turbine blades increases, the demand on the TBCs drastically increases as well [10]. By using TBCs, the cooling effort as well as the metallic temperature of turbine components can be minimized which leads to a further increase in efficiency and component lifetime [11].

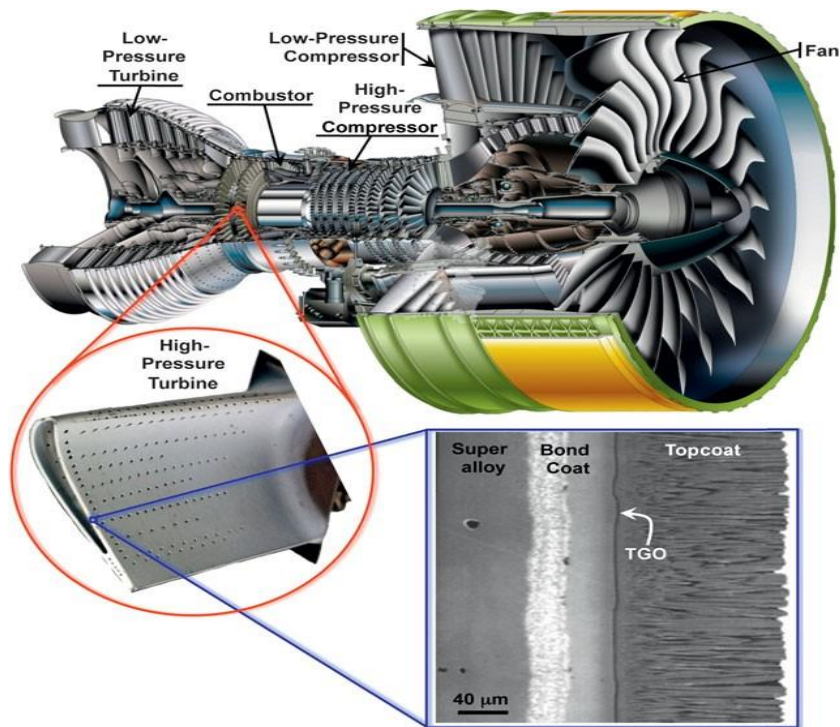


**Figure 2.1:** Cross-section view of Engine Alliance GP7200 aircraft engine, photograph of a turbine blade with thermal-barrier coating, the microstructure shown right to turbine blade is an SEM image of a cross-section of an EB-PVD 7YSZ TBC [1].

Based on various applications, the coatings are deposited by different techniques such as physical vapor deposition (PVD) and plasma spraying [12, 13]. The TBCs are mostly deposited by EB-PVD or by APS. In the EB-PVD process, focused high-energy electron beams are directed to melt and evaporate ingots as well as to preheat the substrate inside the vacuum chamber [13, 14]. During the deposition primary columns start to grow on the substrate surface following a nucleation stage. An equiaxed-zone of grains with no preferred crystal structure

forms initially at the bottom of the deposited coating of specimens (produced under conventional rotating mode and stationary mode). Since the substrate is continuously exposed to vapor flux, shadowed images are only created at line of sight behind grain tips extended slightly from the main column bodies, producing a competitive growth process between columns. This effect governs the appearance of porosity within the coating, (i.e. inter-columnar gaps, voids between feather arms and intra columnar pores) [8]. Due to this TBCs deposited by EB-PVD have a columnar microstructure as shown in the Fig. 2.2 (a). The APS process generates the TBC coating by melting the yttria-stabilized zirconia (YSZ) powder into droplets within a plasma jet and impinging these droplets onto the bond coat surface. A common property of plasma sprayed TBCs is their lamellar structure [15] (see Fig. 2.2 (b)).

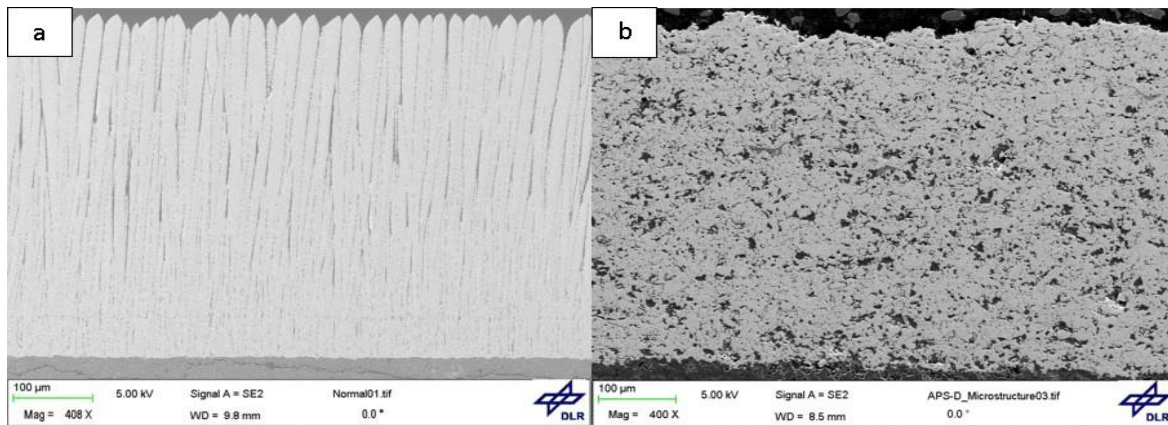


**Figure 2.2:** Scanning electron microscopy image of the cross section of the TBC layer system. (a) EB-PVD morphology of 7YSZ-TBC. (b) microstructure of APS 7YSZ-TBC.

Generally, a TBC system consists of a ceramic top coat, a ceramic thermally grown oxide (TGO), and a metallic bond coat. The top coat provides thermal insulation and consists of ceramic, with low thermal conductivity. Bond coat acts as an intermediate and good adherent nature between top coat and substrate. Bond coat acts as oxidation resistant to the metallic substrate. TGO (Thermal Grown Oxide) forms naturally at high temperatures due to oxidation of the bond coat (Fig. 2.1) [16]. When significant resistance to loading under static, fatigue and creep conditions is required, the nickel-base superalloys have emerged as the base materials of choice for high temperature applications. This is particularly true when operating temperatures are beyond about 800°C [17].

Besides thermal insulation for the metallic components, the TBCs must possess a high strain-compliance to minimize thermal cyclic stresses due to the thermal expansion mismatch with the superalloy material, and must reflect a significant amount of the radiant heat coming from the

hot gases. In addition, TBCs must be able to maintain thermal protection during prolonged thermal cycles and service times pushing the material to work under extreme thermal gradients ( $1^{\circ}\text{C } \mu\text{m}^{-1}$ ) and energy fluxes ( $1 \text{ MW m}^{-1}$ ) without separating from the engine parts [1].

## 2.2 Electron Beam Physical Vapor Deposition (EB-PVD)

EB-PVD is one of the best fabricating thermal barrier coating techniques for turbine blades and vanes of aircraft engines. By the EB-PVD process we can construct an inherent columnar and highly porous microstructure (Fig. 2.3), which is not only beneficial for thermal shock, but also for strain tolerance. The EB-PVD microstructure is favorable due to its low thermal conductivity [18, 19].

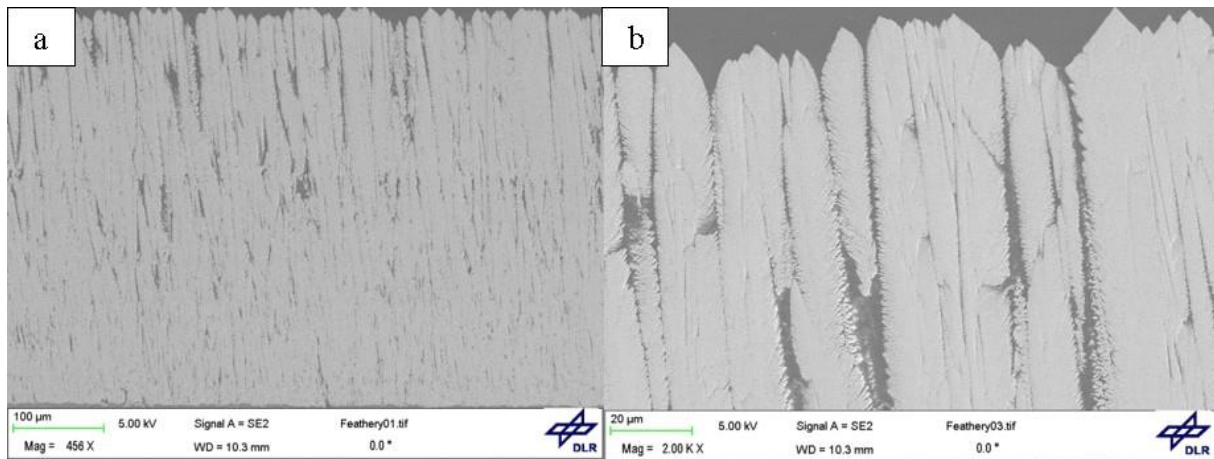


**Figure 2.3:** SEM images of EB-PVD incoherent columnar and highly porous microstructure (a) Low Magnification, (b) high Magnification.

The basic principle of EB-PVD is a form of physical vapor deposition in which a high energetic electron beam targeted towards the ceramic material causes it to melt and vaporise in the form of a cloud within the vacuum chamber. The vapor is deposited onto the substrates at deposition rates of  $\mu\text{m}/\text{min}$ . Coatings with thicknesses up to 100-500  $\mu\text{m}$  can be deposited.

Subject to the substrate material, the substrate pre-heat temperature varies between  $950^{\circ}\text{C}$ - $1050^{\circ}\text{C}$  (Example: for zirconia  $1000^{\circ}\text{C}$ - $1050^{\circ}\text{C}$ ). Additional oxygen is also necessary in order to get the stoichiometric composition of the ceramic coating [5]. The schematic representation of the EB-PVD technique is seen in the Fig. 2.4. EB-PVD typical chamber pressure is around  $10^{-4}$  torr. Typically, the raw materials of the ceramic coatings are in the form of cylindrical ingots or granules. Electron guns with a power rating of 45 kW are common, but electron guns with

greater than 200 kW are also used. The electron beam paths can be changed depending on the required coatings, such as linear, bent or angled (around 270 degrees).

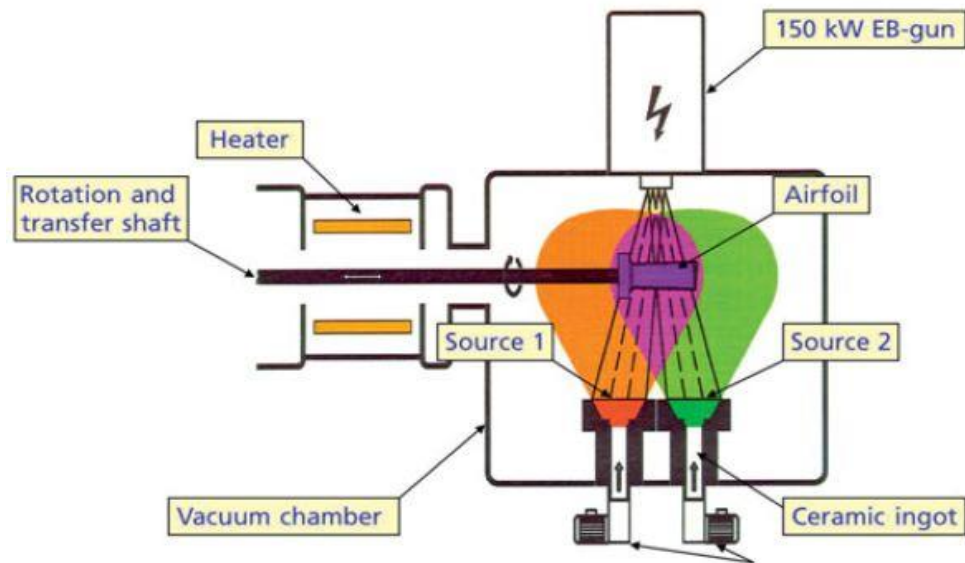


**Figure 2.4:** Schematic representation of EB-PVD technique [5].

Substrates which are to be coated are properly fixed and held over the molten pool in the direction of vaporizing molecules. In order to achieve continuous evaporation, the ingots can be operated by automatic feeder mechanisms to maintain the constant distance between pool and substrate. Multiple layer coatings can be achieved by placing different ingot compositions. This can be obtained by using the jumping electron beam technique. The targeted beam is made to jump alternatively on multiple ingots, promoting the generation of multiple molten pools with different composition [5, 13].

Depending on the requirements, EB-PVD can operate on different modes like stationary, rotating and conventional rotating mode. Complex shaped parts such as turbine blades require tilting and rotation of the parts to create uniform coating thickness. Typical rotation speed is 3 to 30 rpm. Microstructure formed by EB-PVD TBC entirely depends on processing conditions [20].

In conclusion, the primary asset of EB-PVD is the columnar microstructure which contributes strain tolerance and high erosion resistant properties with respect to plasma sprayed TBCs. EB-PVDs also provide a regular surface finish, which is aerodynamically beneficial, as well as a good resistance to thermal shock. Apart from that, EBPVD is of high cost and chemical variability limits due to vapor pressure concern are the deficiencies [5, 19].

## 2.3 Ceramic Topcoat

### 2.3.1 7YSZ

We know that most of the ceramic materials have outstanding properties like low thermal conductivity and high thermal expansion coefficient which are the desired qualities in high temperature application field. YSZ is traditionally confirmed as the standard top coat material due to its superior characteristic profile of low thermal conductivity, relatively high coefficient of thermal expansion, and good thermo-cyclic performance [21]. Zirconia ( $ZrO_2$ ) is a commonly used as a base ceramic material for TBC applications due to its low thermal conductivity compared with other oxides as shown in Fig. 2.5.

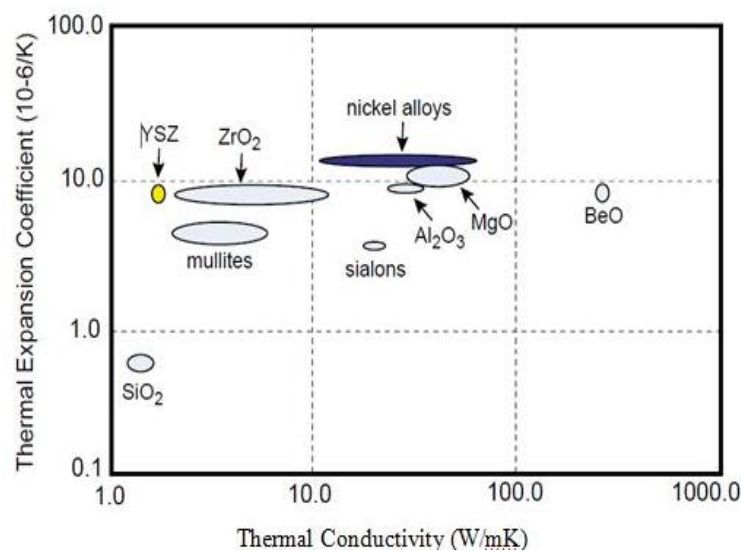


**Figure 2.5:** Thermal Conductivity of distinct oxide materials [22].

Additionally, one of the main characteristic features of zirconia is its polymorph solid (exist in more than one crystal form) nature. Zirconia undergoes phase transformations during heating and cooling as follows (see Fig. 2.6): tetragonal (t) to monoclinic (m) phase change at the temperature 1170°C, cubic (c) to tetragonal (t) phase change at 2370°C, and the melting point is at the temperature of 2690°C [16].

The phase transformation from tetragonal to monoclinic is martensitic in nature, it occurs by small displacements of atoms in the structure. At demanding operational temperatures, the transformation of tetragonal phase to monoclinic damages the lifetime of  $ZrO_2$  based TBCs. During this transformation, a crystal lattice volume change happens generating a volume increase from 3% to 5% causing significant shear strain. Furthermore, an increase of volume to 10% would cause micro cracking, thus damaging the TBC coating [14, 16].

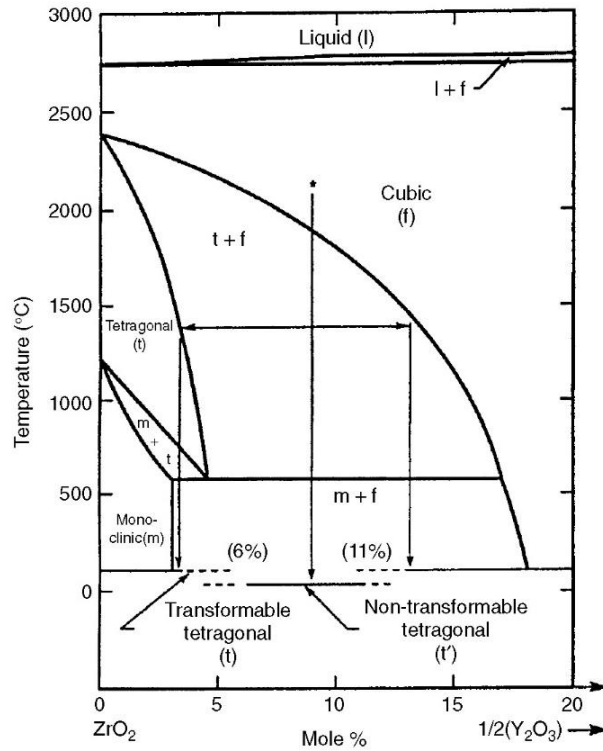


**Figure 2.6:** Phase diagram of Y<sub>2</sub>O<sub>3</sub>-ZrO<sub>2</sub> System [17].

The phase transformation in zirconia can be avoided by alloying with oxides like CaO, MgO, Y<sub>2</sub>O<sub>3</sub>, CeO<sub>2</sub>, Sc<sub>2</sub>O<sub>3</sub> and In<sub>2</sub>O<sub>3</sub>. By adding the mentioned zirconia stabilizers, it inhibits the phase transformation at high temperatures, thus eliminating the volume change. Among the specified alloying oxides, yttria (Y<sub>2</sub>O<sub>3</sub>) forms the most stable solid solution for a ceramic top coat base material for long duration [16].

As the melting point of zirconia is very high it is difficult to melt or vaporize. Thus in order to deposit the coating some less conventional process are used. The best and most reliable coating processes are APS and EB-PVD. As we have already seen above structures formed by these depositing techniques are different. The positive point between yttria and zirconia is having the similar vapor pressure which will be very helpful during the vapor deposition for making the TBC coatings. The approximate content of yttria to stabilize zirconia is 7-8 wt.% [16]. If lower content of yttria is alloyed to zirconia, the transformation to monoclinic phase is not inhibited. The higher yttria content causes cubic phase stabilization with low strength and toughness. With yttria content ranging from 4-10 wt.%, the formed phase is t' as shown in Fig. 2.6, which is known as non-transformable tetragonal, which is stable on cooling without formation of the

monoclinic phase. The phase stability generated by yttria additions to the zirconia ceramic has been the material of choice for modern state of the art TBCs [17].

### **2.3.2 Thermally Grown Oxide (TGO)**

Thermally Grown Oxide forms naturally at elevated temperatures due to oxidation of the bond coat. At high temperatures, the oxygen flows through the top coat by pores, gaps, and micro-cracks towards the bond coat. This is favorable for oxide growth on the bond coat, known as the thermally grown oxide (TGO) layer, which is predominantly  $\alpha$ -Al<sub>2</sub>O<sub>3</sub>. Alpha-alumina is a primary oxide because of its low oxygen diffusivity and superior adherence.

The TGO layer plays an important role in the failure of TBC due to the growth of the TGO layer during oxidation [23]. At first TGO is constrained by TBC and bond coat. In the time where TGO remains fully bonded with TBC and bond coat, it grows by thickening thus causing growing stresses that influence the creep deformation [14]. The TGO layer promotes massive residual compressive stress due to the growth and thermal expansion misfit, causing the layer to be unstable against out-of-plane displacements. The proceeding of the instability is largely dictated by the mechanical characteristics of the bond coat [24].

### **2.3.3 Bond Coat**

The bond coat acts as an intermediate layer between top coat (typically yttria stabilized zirconia) and substrate (typically nickel based super alloy). The typical thickness of the bond coat is between 30-100  $\mu$ m. The most important characteristic that the bond coat should satisfy is a good adhesion property with respect to TBC. It acts as a shield for the substrate when TBC is spalled off during the environmental attack. The bond coat also acts as an oxidation resistor for the substrate [25]. It's also capable of creep and plastic deformation.

Most of bond coats were initially derived from existing environmental coatings and not for the specific requirements of the bond coat. Many new approaches were made to increase the lifetime of TBC by improving the bond coat. Until recently, typical bond coats were PtAl or MCrAlY (M is nickel and cobalt) [26]. In order to provide oxidation resistance, the bond coat has to grow an oxide protective scale during operation. Most of the bond coats contain high level of aluminum to further promote a dense alpha alumina layer ( $\alpha$ -Al<sub>2</sub>O<sub>3</sub>) at the surface of the bond coat bordering to the TBC. The oxide protective scale formed is commonly composed by  $\alpha$ -Al<sub>2</sub>O<sub>3</sub>, which has a relative slow growth rate and is resistant to degradation by any corrosive species

that may reach the surface through the gaps or pores of the thermal barrier coating or subsequent to spallation of the coating [14, 25].

### **2.3.4 Superalloys**

These alloys have been developed for high-temperature service and include iron-, cobalt and nickel based materials, although nowadays they are principally nickel based. These materials are widely used in aircraft and power-generation turbines, rocket engines, and other challenging environments [27]. From the past 50-years nickel-base superalloys have been developed for use in the hot zones of modern gas turbines. Currently, no other commercially available metallic materials are able to offer such a good combination of high-temperature strength and microstructural stability, resistance to fatigue and oxidation as well as high stiffness. Basically there are two main groups of Ni-base superalloys - cast and wrought. Wrought superalloys are usually more ductile than cast alloys. This advantage allows to produce certain larger shapes, such as turbine discs. Cast alloys are normally used, as a structural material for the turbine components with a complicated shape, like blades and vanes. Cast alloys can be polycrystalline as well as single crystal [28]. Although the Ni-based metallic blades are high temperature creep resistant and microstructural stable at temperatures up to 1100°C, they need to be protected by TBCs to keep these temperature conditions within the acceptable levels [8].

### **2.3.5 Alumina (Al<sub>2</sub>O<sub>3</sub>)**

Alumina is one of the best ceramic oxides due to its extensive area of properties. Alumina has a melting temperature of 2072°C and a boiling point of 2977°C. It has a molar mass of 101.96 g/mol and a density of 3.95–4.1 g/cm<sup>3</sup>. Alumina has a high chemical resistance, immense resistivity to thermal shock, high thermal stability, high compression strength, good abrasion resistance, high dielectric strength, and it's also transparent to microwave radio frequencies [29, 30, 31].

Alumina has several metastable crystals. They are  $\eta$ -,  $\gamma$ -,  $\delta$ -,  $\theta$ -, and  $\alpha$ -alumina [32]. The approximate temperatures required for crystalline phase transformation of alumina are  $\gamma \rightarrow \delta$  (850°C);  $\delta \rightarrow \theta$  (1100°C);  $\theta \rightarrow \alpha$  ( $\geq 1200^\circ\text{C}$ ) [32]. The phase transformation of alumina with respect to temperature manufactured by different techniques is shown in the Fig. 2.7. Alumina can exist in different phases depending on its purity and mechanical and physical properties [33].

Out of all the phases,  $\alpha$ -alumina is the most thermodynamically stable phase of alumina.  $\alpha$ - $\text{Al}_2\text{O}_3$  consists of hexagonal crystal structure with lattice parameters of  $a=4.758 \text{ \AA}$  and  $c= 12.991 \text{ \AA}$  [30, 34].  $\alpha$ -alumina is the most stable polymorph which crystallizes at high temperatures. Due to its high temperature resistant property it can be operated in high temperature applications. The thermodynamic stable  $\alpha$ - $\text{Al}_2\text{O}_3$  can be used as a coating material because of its vast range of properties like high wear resistance, good thermal shock resistivity, high hardness, and good chemical resistance [29, 30].

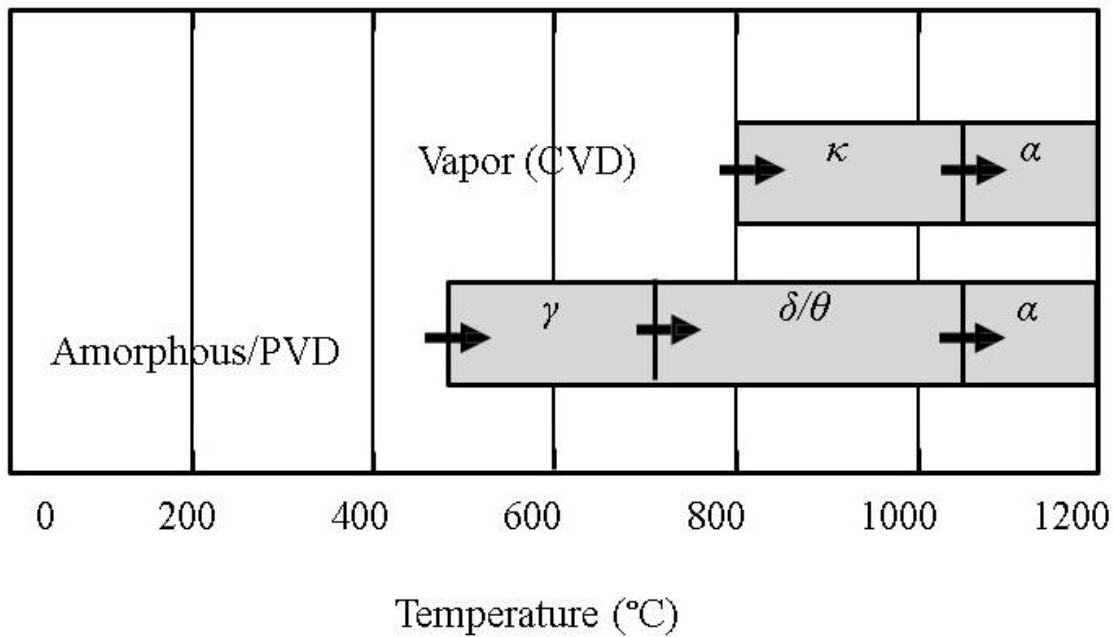


**Figure 2.7:** Alumina phase transition at different temperatures by different depositing techniques [33].

In modern times, composite layers of  $\text{Al}_2\text{O}_3/\text{YSZ}$  coatings on thermal barrier coating substrates have been proposed [11, 12]. In these coatings, due to existence of  $\text{Al}_2\text{O}_3$  layer as top coat, oxygen or other factors which are disturbing the infiltration are reduced and formations of TGO and zirconia phase transition are retarded. By these composite type of layers  $\text{Al}_2\text{O}_3/\text{YSZ}$  further improvement of thermal and mechanical properties of TBCs can be achieved, but the effect of other parameters such as the type of composite are yet to be studied [35, 36].

Alumina coating was achieved on top of 7YSZ by magnetron sputtering, electrophoretic deposition (EPD) and plasma spraying [9, 37, 38, 39]. A very thin alumina layer (thickness of 5 to 8  $\mu\text{m}$ ), deposited by EB-PVD as a bond coat, was observed [40]. It is also important to emphasize that no results have been published until now with the use of EB-PVD alumina top coatings (with thickness 120  $\mu\text{m}$ ) for CMAS infiltration studies. So by fabricating EB-PVD

alumina, which acts as a CMAS resistant layer, it can be used in a new multilayer coating for aero-engines thus inhabiting further infiltration.

## 2.4 Calcium Magnesium Alumina Silicate (CMAS)

Many of the elements in the earth's crust and soil occur in the form of minerals, which mainly consists of oxygen, silicon, calcium, magnesium, iron and aluminum elements, giving the scope for the formation of CMAS a wide range of locations. As per the literature survey, many of the TBC coated engine parts are subjected to sand particles, which further promote the failure of TBCs or hinder their lifetime. A keen observation of affected TBC components will give an overview of the elements deposited on the TBC; typically, CaO, MgO, Al<sub>2</sub>O<sub>3</sub> and SiO<sub>2</sub> [41].

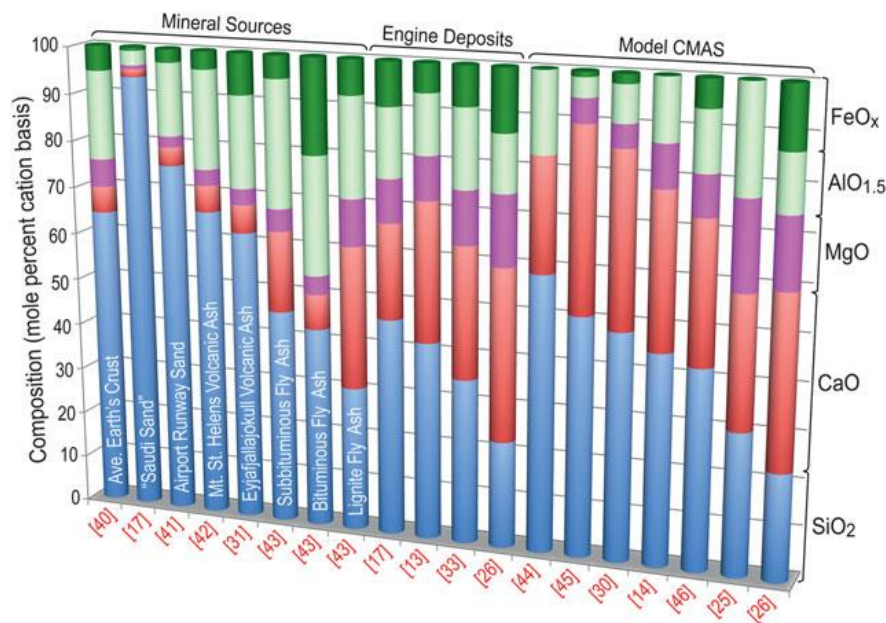


**Figure 2.8:** Compositions of calcium-magnesium-aluminum-silicates of mineral sources, engine deposits and laboratory model CMAS [42].

The intake of these CMAS compositions with air into the combustion process of aero gas turbine engines increases the engine's sensitivity to thermomechanical failure during repeated thermal cycling (Heating and cooling) [43]. When the surface of a TBC exceeds the CMAS melting temperature, the deposits can melt and partially infiltrate into the ceramic microstructure. When enough CMAS is available on the surface, it will infiltrate into the TBC until it reaches a lower temperature that raises the glass viscosity and stops the infiltration. The temperature at which the CMAS infiltration ceases is near the lower eutectic, approximately 1170°C. A typical melting temperature of CMAS is in between 1100°C to 1250°C [44]. TBCs can tolerate limited CMAS infiltration of approximately 50 μm [14].

The presence of these mineral particles in engine components at low temperatures generates erosive wear on the TBC, whereas that molten CMAS at high temperatures generates detrimental thermo-mechanical and thermo-chemical effects, thus reducing their service life. In general, the elemental composition and the melting temperature of CMAS depend on the geographical presence (see Fig. 2.8) [14, 42]. The below Fig. 2.9 gives an idea about a volcanic ash erupted zone and engines operated in a desert area.

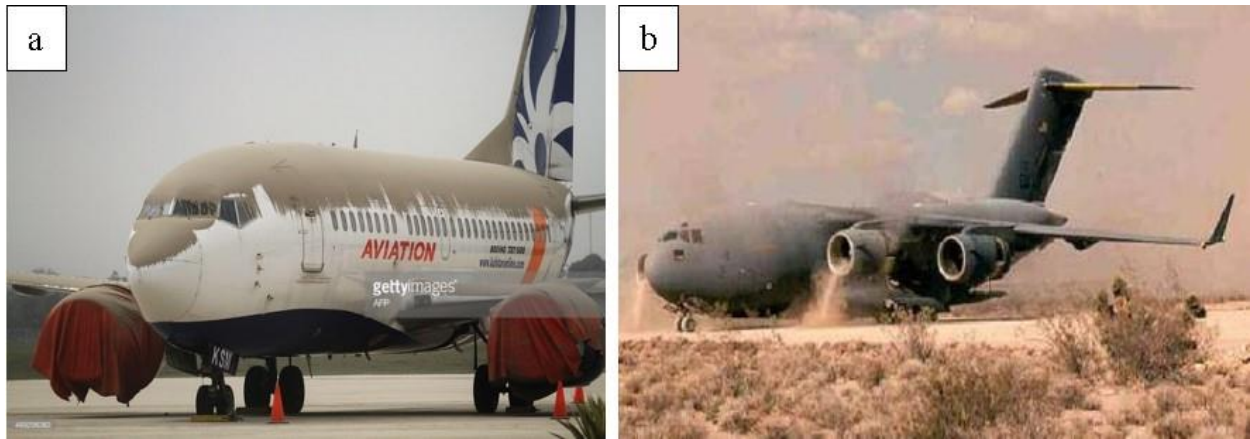


**Figure 2.9:** (a) Plane covered by ash was shut down during the volcanic eruption at solo in Central Java in 2014, (b) operational flight at desert areas.

#### 2.4.1 Thermochemical Attack

When the 7YSZ TBC is exposed to CMAS the coating partially dissolves in the CMAS at high temperature region, causing disruptive phase transformation (from tetragonal,  $t$   $ZrO_2$  to monoclinic,  $m$   $ZrO_2$ ). The tetragonal to monoclinic phase transformation causes a significant volume change (increases up to 5%). Due to this phase transformation stress localization occurs in the TBC eventually causing the coating spallation [45].

#### 2.4.2 Thermomechanical Attack

At the operating temperatures of aero-gas turbine engines, the ingested CMAS particles melt and infiltrate into the pores and columnar gaps (of EB-PVD and APS TBCs) under capillary forces. CMAS viscosity, surface tension, and TBC permeability are the main mechanisms governing the CMAS infiltration into the porous TBC structure. The crystallization of the CMAS melt generates stiffening of the TBC structure leading to a loss of strain tolerance during cooling which creates a ceramic coat delamination. The complete CMAS infiltration leads not only to stiffening of the coating, but also to degradation of the insulating properties of the TBC [42]. Once the CMAS infiltrated TGO is exposed to thermal cycling, the thermal expansion

coefficient (TEC) between the bond coat and the ceramic coat is altered. The TBC mismatch between both layers generates a higher strain rate during cooling leading to TBC spallation [46].

## **2.5 Efforts in restricting CMAS induced damage in TBCs**

The infiltration of CMAS melts on standard 7YSZ TBCs bring detrimental effects on the lifetime of the coatings; other approaches for CMAS arrest have been proposed [47]. Most of the proposed approaches for CMAS mitigation focus on the chemical reaction generated between the CMAS melt and the TBC by mostly following two mitigation procedures:(a) Stop the melt by crystalizing its main constituents (mostly silicates) and therefore, elevating their melting temperature, and (b) to fill the pores and columnar gaps with the new crystalized phases in order to block any excess melt into the TBC [42]. A lot of efforts were done in the literature to study the mitigation of CMAS with different TBCs. Few among those are mentioned here such as EB-PVD 7YSZ, 14YSZ, HfSZ, 29DySZ, CeSZ, and Gd<sub>2</sub>Zr<sub>2</sub>O<sub>7</sub> were tested against CMAS/VA attack given relatively harsh thermal loading conditions of 1260 °C for 2 h. most coatings were left completely infiltrated via TBC dissolution–precipitation processes and formation of new zirconia-rich phases preferably at the column tips and within the inter-columnar gaps except GdZ. This implies a low chemical reactivity of the zirconia-based materials with CMAS while the propensity to infiltration is high, regardless of tetragonal or cubic zirconia polymorphs in the top coat, and nearly independent of the amount and type of stabilizing ion in the zirconia lattice [48].

Lanthanide magnesium hexa-aluminate (LaMgAl<sub>11</sub>O<sub>19</sub>) is another promising TBC ceramic candidate that was also tested against CMAS attack. However, it does not lead to crystallization for the lack of Al, leaving the difficult-to-crystallization glass composition of CMAS [49]. GdZ is the only one which worked better up to now and utilising in present air-craft engines. However, AVA reaction with GdZ leads to formation of a new phase which contains high amounts of Zr, Gd and Fe [48]. The main disadvantage is a long-term mitigation of AVA infiltration may be not achievable for Gd<sub>2</sub>Zr<sub>2</sub>O<sub>7</sub> TBCs. This is mainly due to large solid-solution ranges of key reaction products, resulting in dynamic, permanently evolving chemical equilibria [50].

### **2.5.1 EB-PVD Alumina top coat as a CMAS restricting TBC**

The use of EB-PVD alumina topcoat (thickness of 120 µm) for CMAS mitigation has not been researched yet. However, available publications in this field have shown promising results as far

as effectiveness for CMAS mitigation with APS coatings [4]. Thermochemical interaction between CMAS and APS alumina ( $\alpha$ -Al<sub>2</sub>O<sub>3</sub>) leads to the formation of anorthite (CaAl<sub>2</sub>Si<sub>2</sub>O<sub>8</sub>, 1553°C) and spinel (MgAl<sub>2</sub>O<sub>4</sub>, 2135°C) phases with high melting points and good chemical stability which act as a CMAS crystallization product [4, 39].

## **2.6 Sintering Effect**

The resulting lifetime of TBCs not only depends on microstructure or processing, but also on the kinetics of degradation of the TBCs. Ceramic material properties change at high temperatures for long duration of time, which affects the performance and durability of TBC components. One of the major effects at high temperature operation of ceramics is sintering. Sintering causes increase in stresses, thermal conductivity, and thermal shock which abnormally impact their reliability [19, 51, 52]. Several studies were inspected on aero engine parts, where TBC (for ceramic top coat) degradation had taken place because of heavy sintering and increased thermal stresses during operation of the engine.

## **2.7 Reaction Bonded Alumina oxide (RBAO)**

RBAO acts as a multifunctional coating for porous fiber reinforced oxide composites. RBAO from Al metal and Al<sub>2</sub>O<sub>3</sub> powders is a well-established processing method for alumina based ceramics and composites (CMCs) fabricated by a simple painting and firing process. RBAO process is performed at moderate temperatures of 1350°C in air. The RBAO top coats exhibits excellent adherence and provide smoothing and stabilization of the surface and also acts as erosion and wear protection. RBAO coatings can be employed as bond-coats for additional environmental barrier top coats [53].

## Chapter 3: Experimental Procedure

### 3.1 EB-PVD Al<sub>2</sub>O<sub>3</sub>/7YSZ TBC preparation

Al<sub>2</sub>O<sub>3</sub> as a top layer was deposited on the previously coated 7YSZ TBCs via EB-PVD process using a “von Ardenne Anlagentechnik GmbH” 150 kW pilot plant with single gun dual source coater (see Fig. 3.1). It consists of three different chambers for loading, preheating, and deposition in various atmospheres up to 10 Pa. The ability to co-evaporate from two independent sources with one gun is maintained by a rapid beam deflection system in combination with a sophisticated control system for gun power, beam pattern, beam focus, and other electron beam parameters. The gun can be operated at different accelerating voltages up to 40 kV while power is controlled by vario-cathode. The ingots of various diameters were bottom feed into water cooled copper crucibles. For more details, refer to [36, 54].



**Figure 3.1:** EB-PVD 150 KV von Ardenne Anlagentechnik GMBH pilot plant [8].

To avoid damage of metallic substrates (nickel based super alloys) and bond coats during the high temperature infiltration tests for long duration, alumina substrates of 1mm thickness were used as a base material to deposit Al<sub>2</sub>O<sub>3</sub>/7YSZ TBCs. A high energetic electron beam targeted towards the 7-8 wt. % Y<sub>2</sub>O<sub>3</sub> stabilized ZrO<sub>2</sub> ingots, which causes 7YSZ ingots to melt and starts vaporising in the form of a cloud within the vacuum chamber. The 7YSZ vapor is deposited onto the alumina substrates. A parameter study was conducted for EB-PVD alumina topcoat on 7YSZ TBC and different runs were made and the results will be explained in the next sections. Fig. 3.2 shows the obtained microstructures for the as-coated samples. The deposited EB-PVD 7YSZ and alumina top coat comprised with a thickness of around 150-160 μm and 100-120 μm, respectively.

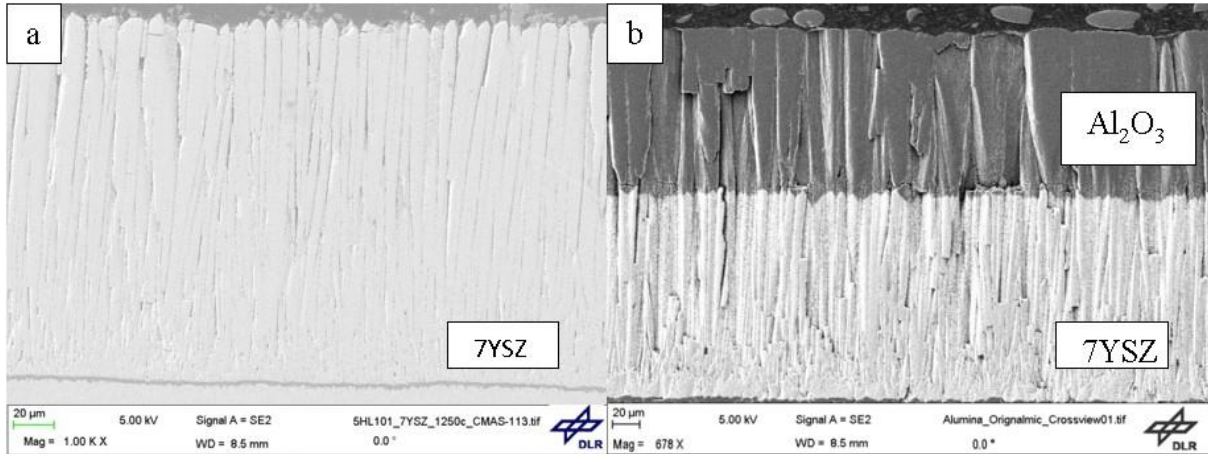


**Figure 3.2:** (a) SEM image of EB-PVD 7YSZ TBC coating, (b) EB-PVD Alumina/7YSZ coating.

### 3.2 CMAS and Volcanic ash compositions

In the section 2.4, it clearly shows that there exists a high variation in the CMAS compositions depending on the geographical presence (see Fig. 2.8). Two different CMAS compositions and one natural volcanic ash (VA) were used in this study. Both CMAS powders (CMAS1 and Krämer CMAS) were artificially synthesized in the laboratory as used in previous studies [44, 55, 56]. The volcanic ash used during the experiments were collected from site erupted from the Eyjafjallajökull volcano in Iceland in 2010 [57].

**Table 3.1** Chemical Composition of CMAS1, Krämer CMAS and Iceland Volcanic ash

CMAS/VA	Chemical Composition (wt. %)								Crystalline phase	Melting Point, °C
	CaO	MgO	Al <sub>2</sub> O <sub>3</sub>	SiO <sub>2</sub>	FeO	TiO <sub>2</sub>	Na <sub>2</sub> O	K <sub>2</sub> O		
CMAS1	22	8	18	40	10	2	-	-	Pyroxene + Anorthite	1225°C-1250°C [15]
Krämer CMAS	33	9	13	45	-	-	-	-	Amorphous	1235°C-1240°C [56]
Iceland Ash	11	4	11	46	20	5	1.94	0.96	Amorphous + some crystalline phases	1150°C [57]

The chemical compositions of CMAS1, Krämer CMAS and Iceland ash (VA) is shown in the Table 3.1. From the table, a significant difference in the SiO<sub>2</sub> content can be seen between VA and CMAS composition. So VA is rich in SiO<sub>2</sub> and CMAS are rich in CaO. Krämer CMAS doesn't contain any FeO. The FeO and TiO<sub>2</sub> content in Iceland ash is much higher than in CMAS1 which might play a key role will be discussed in further sections.

### 3.3 X-Ray Diffraction Analysis

XRD analysis was used to categorize the phase formation, crystal structure of different crystalline phases and reactions within CMAS and alumina layer [58]. The XRD powders were mixed with a 60 wt. % composition of CMAS/VA powder and 40 wt. % of alumina powder on platinum sheets as shown in Fig. 3.3 (a). The samples were isothermally heat treated at temperature 1250°C for 10 hours at a heating rate of 10K/min. After heat treatment the reacted powders were finely grinded and prepared for XRD analysis (maximum 2 μm, Fig. 3.3 (b)).

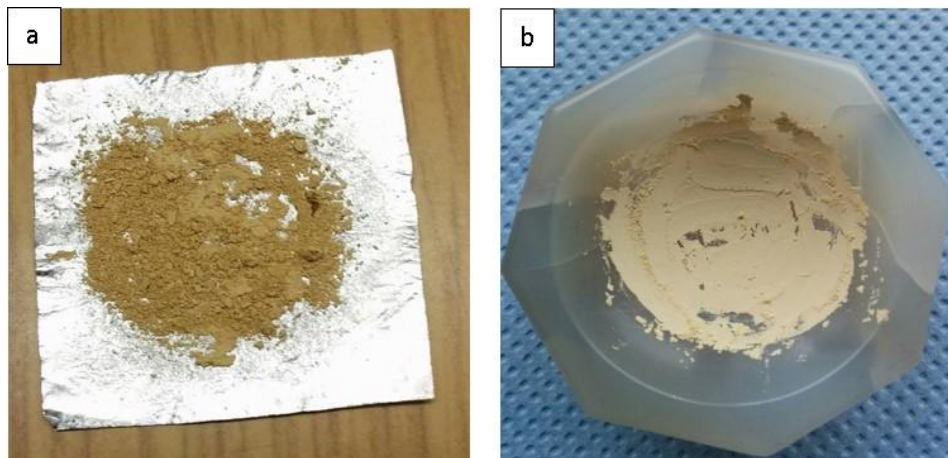


**Figure 3.3:** (a) XRD powders ready for heat treatment placed on platinum plate. (b) XRD powders were finely grinded after heat treatment.



**Figure 3.4:** CMAS/Alumina mixture deposited on XRD sample holder.

The grinded CMAS/Alumina powder processed like a paste and deposited on a XRD sample holder as shown in Fig. 3.4. XRD analyses were performed using Siemens D5000 diffractometer using Cu-K $\alpha$  radiation with a secondary graphite monochromator and Diffrac.EVA software (EVA/Topas 4.2 software package, Bruker Karlsruhe, Germany).

### 3.4 Infiltration Tests

#### 3.4.1 Short Term CMAS Infiltration tests for Alumina/7YSZ Coatings

The short term infiltration tests were done to understand the initial stages of reaction. The short term infiltration tests were carried out in a thermal cyclic furnace. Standard EB-PVD Alumina/7YSZ coatings were used for rapid CMAS infiltration tests. Infiltration samples were prepared by depositing the CMAS amount of 20mg/cm<sup>2</sup> on the Alumina top coated samples. The samples were kept and heated at a temperature of 1250°C for short term intervals (2 and 5min). Fig. 3.5 shows the CMAS deposited samples before and after the heat treatment.

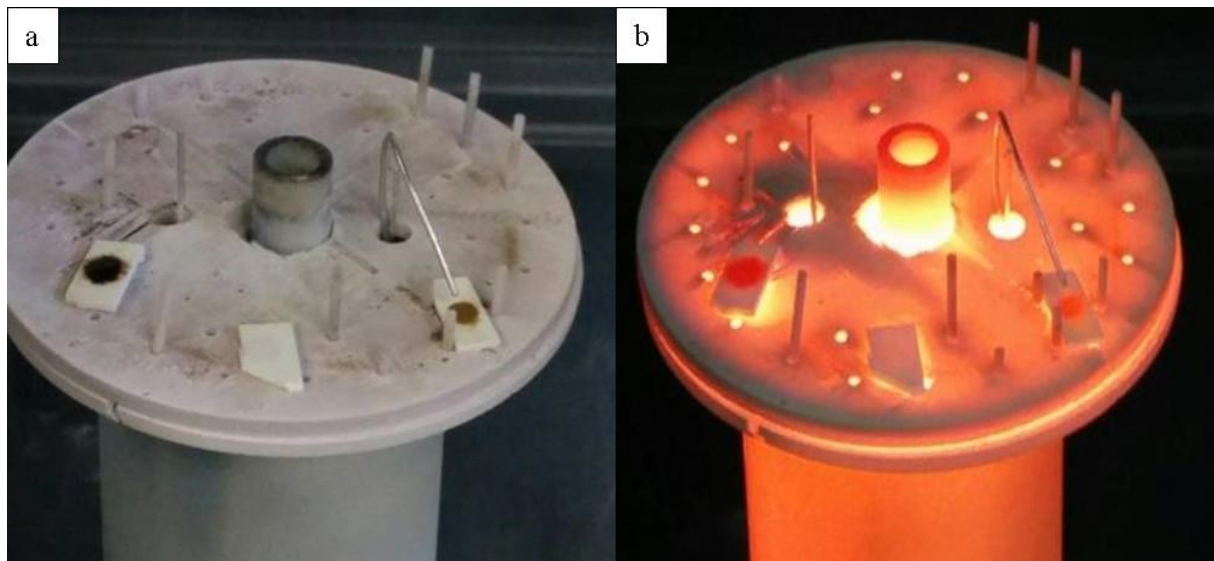


**Figure 3.5:** Samples placed in thermal cyclic furnace sample holder (a) before heat treatment, (b) after heat treatment.

The cyclic furnace was calibrated by preheating the furnace chamber to 1250°C for 1 h. before placing the samples on it. The sample temperature was measured with a thermocouple placed next to the surface of the coating during the heating process. After 1 h. preheating of the loading chamber, the samples were loaded into the furnace and the heating profile was measured as shown in Fig. 3.6. The heating profile shows an overall time of 480 sec. (8 min.)  $\pm$  15 sec. for the sample to reach 1250°C. The heating time was set for 13 min. (780 sec.) after sample loading which provides a temperature of 1250°C for 5 min.

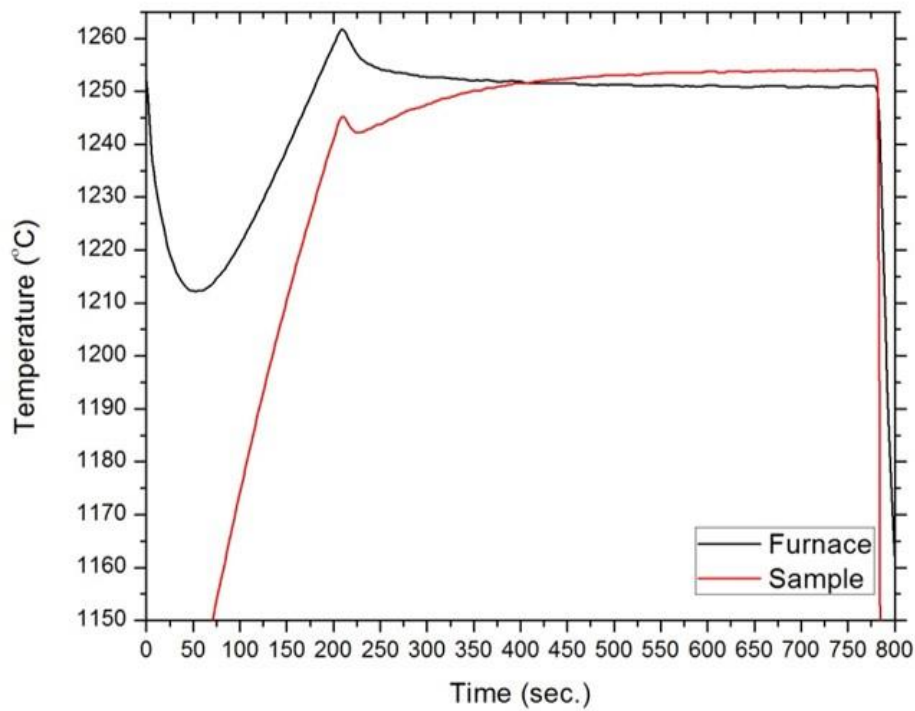


**Figure 3.6:** Thermal profile (Time vs Temperature) of the furnace and sample for short term infiltration tests.

### 3.4.2 Long Term CMAS Infiltration tests for Alumina/7YSZ Coatings

Long term CMAS infiltration experiments were carried out isothermally at temperatures of 1225 and 1250°C in a Netzsch chamber furnace for different times. CMAS in the amounts of 20mg/cm<sup>2</sup> were deposited on the alumina/7YSZ samples. Fig. 3.7 shows the alumina top coated samples before and after heat treatment.

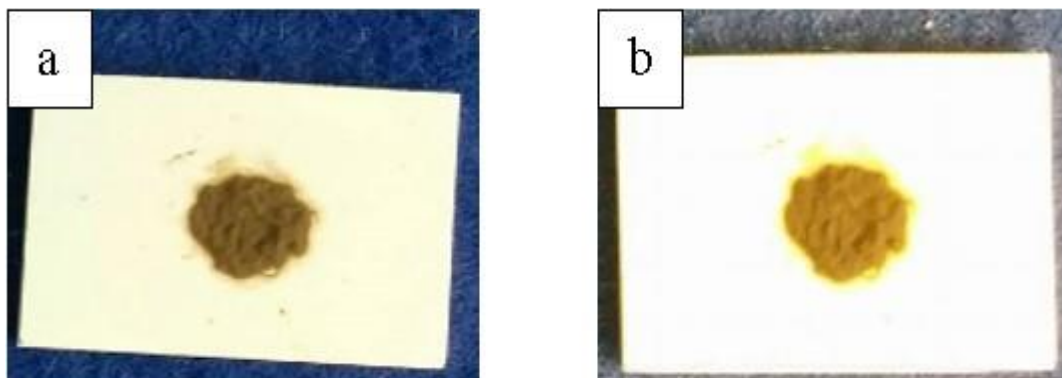


**Figure 3.7:** CMAS deposited alumina/7YSZ samples (a) before and, (b) after the heat treatment.

### 3.5 Manufacturing of RBAO on EB-PVD Alumina/7YSZ TBC

RBAO topcoats were fabricated by a simple painting and firing process. Starting material as spray-atomized Al powders (70 vol %) and  $\alpha$ -Al<sub>2</sub>O<sub>3</sub> (30 vol %) powders were used for the RBAO processing. Soluble polymer (polyvinylpyrrolidone) of 5 wt. % was added to the powder mixture. The powders were dispersed in isopropanol and homogenized ultrasonically for 5 min (30 wt. % solid content). EB-PVD Alumina/7YSZ TBCs were cleaned ultrasonically in deionized water and dried carefully.

The green coatings were deposited on the alumina topcoat TBCs by painting with a hairbrush (Fig. 3.8 (a)). After painting, EB-PVD alumina top coat was completely covered. After drying, the coated samples were heat treated for 1 h at 1350°C with a heating rate of 10°C/min in isothermal furnace (Fig. 3.8 (b)). After heat treatment,  $\alpha$ -Al<sub>2</sub>O<sub>3</sub> was created, because transformation to  $\alpha$ -Al<sub>2</sub>O<sub>3</sub> advances at high temperatures exceeding 1200°C [32, 59].

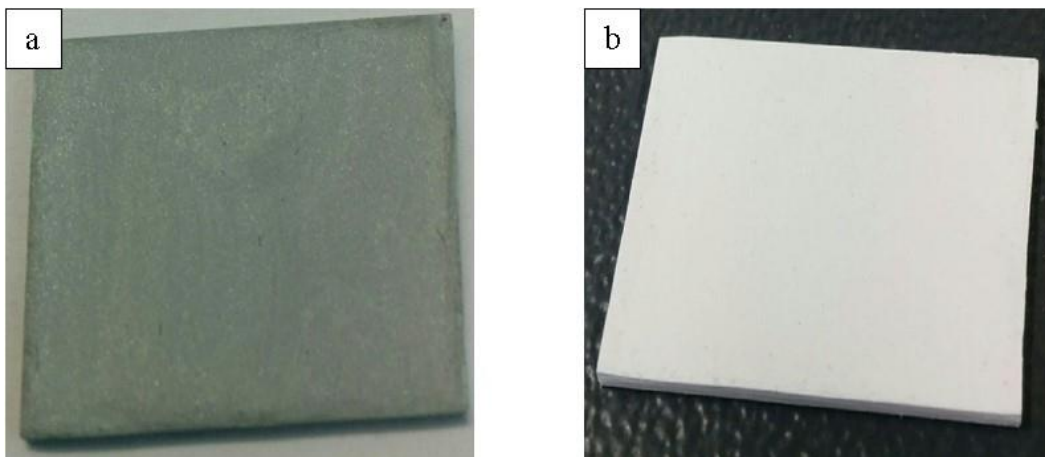


**Figure 3.8:** (a) RBAO precursor, (b) RBAO coated surface after heat treatment.

Fig. 3.9 shows the fabricated RBAO on top of EB-PVD alumina. The obtained thickness was around 20-25  $\mu$ m. After reaction bonding process, the microstructure with no macroscopic crack formation or RBAO coating - alumina topcoat de-bonding was observed.

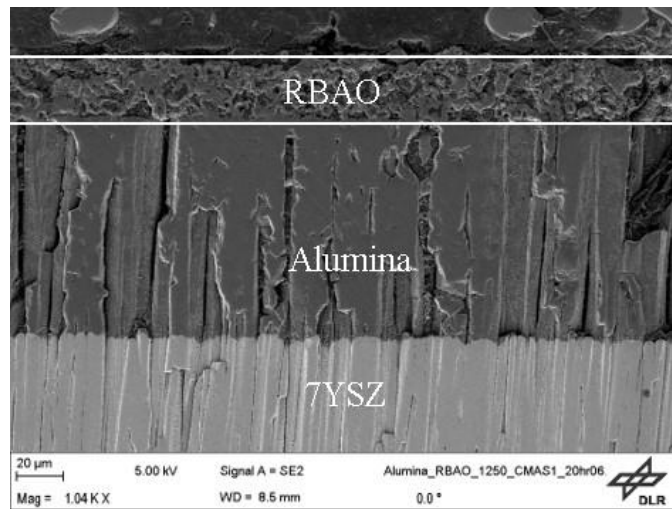


**Figure 3.9:** Cross section SEM micrograph of RBAO Alumina/7YSZ.

### **3.6 Characterization of CMAS Infiltrated Samples**

The samples after CMAS infiltration tests were metallographically prepared. To analyze the CMAS infiltrated samples standard metallographic techniques were used. To study and analyze the reaction zones and infiltration depth, Scanning Electron Microscopy (SEM) (DSM ultra 55, Carl Zeiss NTS, Wetzlar, Germany) was used. The identification of chemical composition was carried out by energy-dispersive spectroscopy (EDS) (Inca, Oxford Instruments, Abingdon, UK).

## Chapter 4: Experimental Results

### 4.1 Fabrication of EB-PVD Al<sub>2</sub>O<sub>3</sub> on top of 7YSZ TBCs

#### 4.1.1 Manufacturing the EB-PVD alumina top layer on 7YSZ

The phase content and morphology of alumina depends on process parameters, primarily substrate temperature, chamber pressure, and deposition rate [9, 40]. It was known from the literature that increasing the beam power in order to raise the substrate temperature for in situ deposition of  $\alpha$ -alumina has resulted in an unstable melt pool and melt spitting [9]. During the deposition of the EB-PVD alumina coatings at DLR, similar circumstances were observed. A parameter study was conducted by varying the important parameters such as sample temperature, pressure and rotation speed and corresponding Al<sub>2</sub>O<sub>3</sub> microstructure was investigated under SEM.

The 7YSZ coated TBCs were fixed on a six flat edge rotating horizontal holder which was perpendicular to the ingot axis. They were homogeneously pre-heated to 890-1000°C according to the desired final substrate temperature for approximately 10 min. There by 7YSZ coated TBC samples were ready for alumina deposition. The deposition was carried out by single source evaporation under conventional rotating mode at different temperatures and pressures for the same rotation speed, as reported in Table 4.1.

**Table 4.1** Processing Parameters of EB-PVD alumina on top of 7YSZ TBCs

Runs	Probe Temperature(°C)	Pressure (mbar)	Rotation Speed (rpm)	Coating Thickness ( $\mu\text{m}$ )
Run 1	890 $\pm$ 5	6*10 <sup>-3</sup>	12	40 $\pm$ 10
Run 2	775 $\pm$ 5	6*10 <sup>-3</sup>	12	26 $\pm$ 5
Run 3	780 $\pm$ 10	9*10 <sup>-3</sup>	12	58 $\pm$ 5
Run 4	810 $\pm$ 10	9*10 <sup>-3</sup>	12	110 $\pm$ 10

Fig. 4.1 shows the SEM micrographs of the manufactured alumina layers with respect to their coating parameters. The resulting morphology in terms of column diameter and size can be seen in the figure. With probe temperature (890 $\pm$ 5) and pressure (6\*10<sup>-3</sup>), Run 1 shows that the morphology comprises of irregular and asymmetrically distributed primary columns (see Fig.4.1 (a)). The coatings obtained after Run 1 were very brittle with relatively low density. Run 2 was

performed by decreasing the sample temperature and maintaining the same chamber pressure as in Run 1. These coatings show uniform growth as columnar structure (Fig. 4.1 (b)), but they were brittle. By maintaining the same sample temperature and increasing the pressure, Run 3 was performed. The obtained coatings were of uniform thickness with desired density of columns, but wider inter-columnar gaps were observed. Run 4 was employed with slight increase in sample temperature and same chamber pressure as in Run 3. The coatings show regular growth of columns with less inter-columnar gaps. A uniform thickness with desired density was achieved. Run 4 coatings were selected for all the further infiltration tests (see Fig. 4.1 (d)).

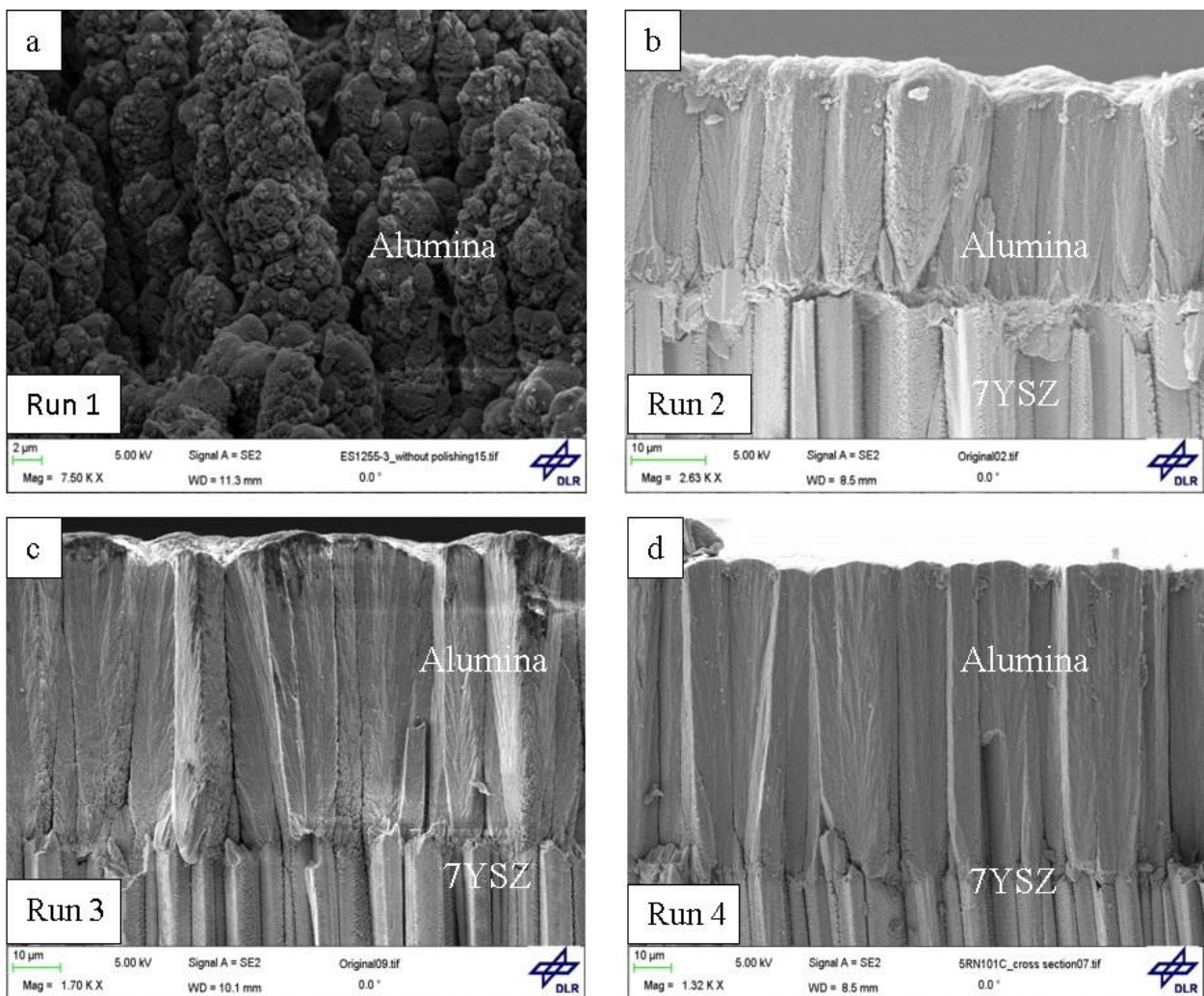


**Figure 4.1:** Fractured SEM micrographs of alumina/7YSZ EB-PVD coatings in as-coated conditions after (a) Run 1, (b) Run 2, (c) Run 3 and (d) Run 4.

#### 4.1.2 Alumina Phase characterization and transition using In-situ XRD

As coated EB-PVD alumina coatings were amorphous in nature. Among the large variety of alumina polymorphs,  $\alpha$ -alumina is the most desirable phase because of its low oxygen diffusivity and high thermal stability in the high temperature range [9]. It was found out that the phase transformation of alumina with respect to temperature changes by different techniques is shown in [60]. In order to identify the alumina phase transformation, In-situ high temperature XRD was done on as-coated samples. It is known from the existing literature that phase transition from amorphous to crystalline  $\alpha$ -alumina occur in the temperature range of 900°C to 1200°C [9]. High temperature XRD was done from 900°C to 1200°C in steps of 50°C raise in temperature maintaining for 30 min holding time. From the Fig. 4.2 change in the  $\alpha$ -alumina peak intensities can be clearly seen.

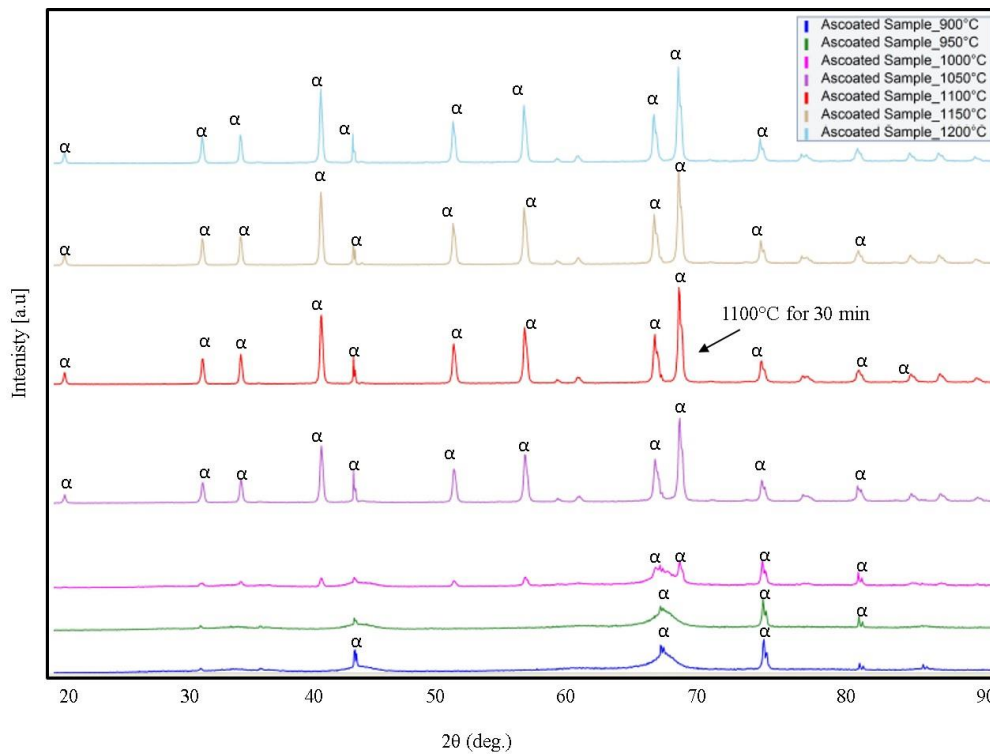


**Figure 4.2:** In-situ high temperature XRD for as-coated alumina substrate.

From 900°C to 1050°C the peak intensities of  $\alpha$ -alumina were very low. High intensity peaks of  $\alpha$ -alumina were observed at 1100°C for 30 min. Thus, this temperature was taken into consideration for further heat treatment of as-coated samples to develop thermodynamically stable  $\alpha$ -alumina topcoat.

### 4.1.3 Sintering effect on the morphology of EB-PVD $\text{Al}_2\text{O}_3/\text{7YSZ}$ TBCs

During the isothermal heat treatment in order to achieve the crystalline  $\alpha$ -alumina, heavy sintering of the coating was observed. SEM micrographs in Fig 4.3 show the drastic change in microstructure before and after heat treatment. As-coated samples at room temperature are fully dense with less inter-columnar gaps and pores (Fig.4.3 (a) and Fig. 4.3 (b)). After the heat treatment ( $1100^\circ\text{C}$  for 30 min) inter-columnar gaps widened by 2-4 % in the alumina top coat (Fig.4.3 (c) and Fig. 4.3 (d)).

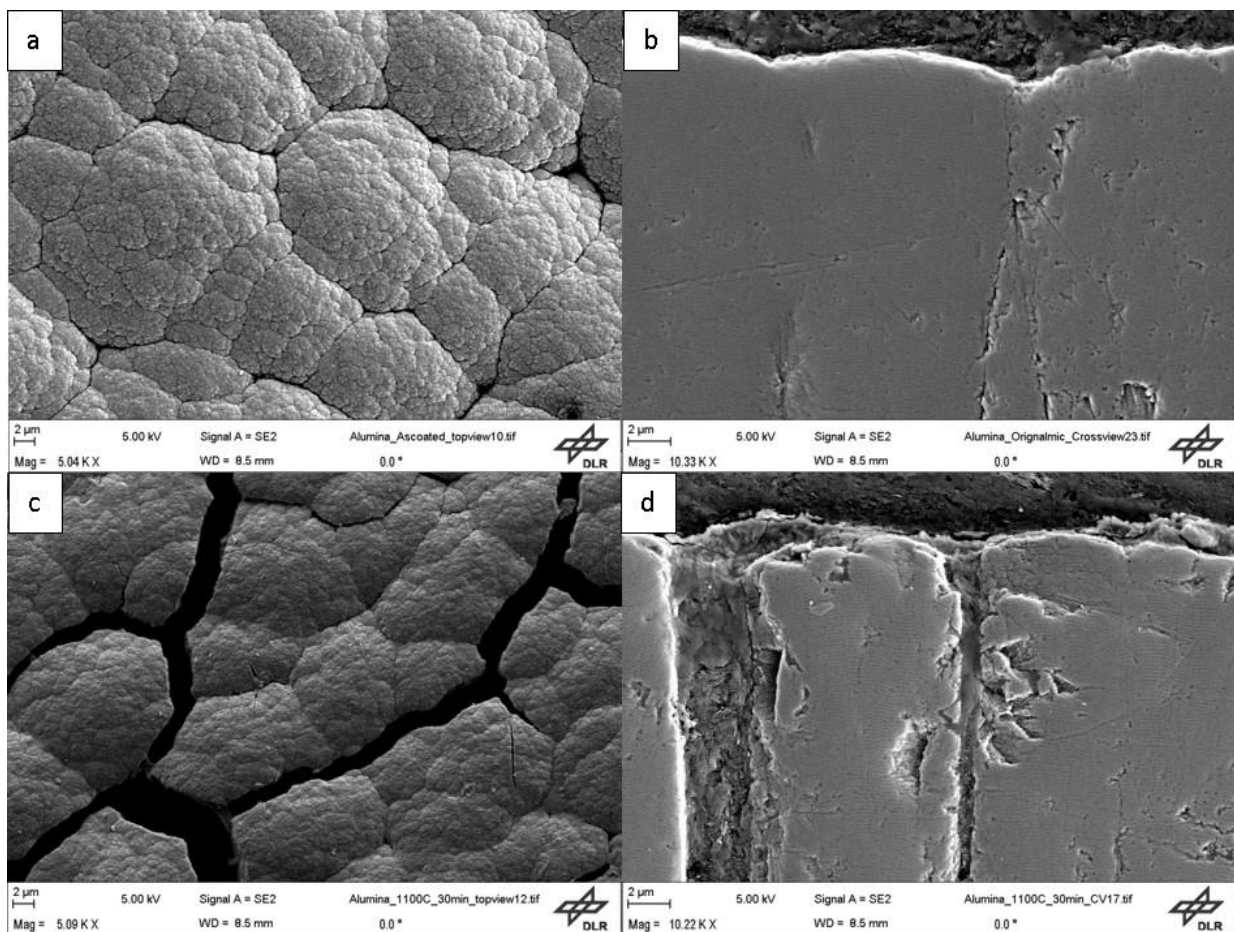


**Figure 4.3:** (a) and (c) are the SEM micrographs taken on the top surface of the coating, before and after the heat treatment, (c) and (d) are the cross-sectional images of the polished  $\text{Al}_2\text{O}_3$  samples after heat treatment.

#### 4.1.4 Phase characterization of CMAS and volcanic ash alumina powders

Fig. 4.4 shows the XRD pattern of the reacted alumina with the CMAS/VA powders (heat treated at 1250°C for 10 h). Al<sub>2</sub>O<sub>3</sub> has reacted firmly with the CMAS/VA mixtures and formed stable phases. Two main phases are identified as anorthite (+) and spinel (#) which are shown on the top right side of the Fig. 4.4. The both formed phases i.e., anorthite (+) and spinel (#) exhibits CMAS sealing property for alumina coatings [37].

Anorthite (+) exhibits the highest peak intensity for Krämer CMAS, followed by CMAS1 and Iceland ash at the end. For all the CMAS/VA compositions, the anorthite (CaAl<sub>2</sub>Si<sub>2</sub>O<sub>8</sub>) phase exists. The second common phase, identified as spinel (MgAl<sub>1.9</sub>Fe<sub>1</sub>O<sub>4</sub>), exists in CMAS1 and Iceland ash.

In Krämer CMAS alumina mixture, an additional phase is identified as gehlenite (Ca<sub>2</sub>(Mg<sub>0.25</sub>Al<sub>0.75</sub>)(Si<sub>1.25</sub>Al<sub>0.75</sub>O<sub>7</sub>)) which might be left over CMAS glass. In the case of Iceland ash, pseudobrookite (Fe<sub>2</sub>TiO<sub>5</sub>) containing Fe and Ti was identified. Note that the α-alumina peak in Iceland ash is from alumina substrate material (XRD was directly done on the VA deposited as coated sample).

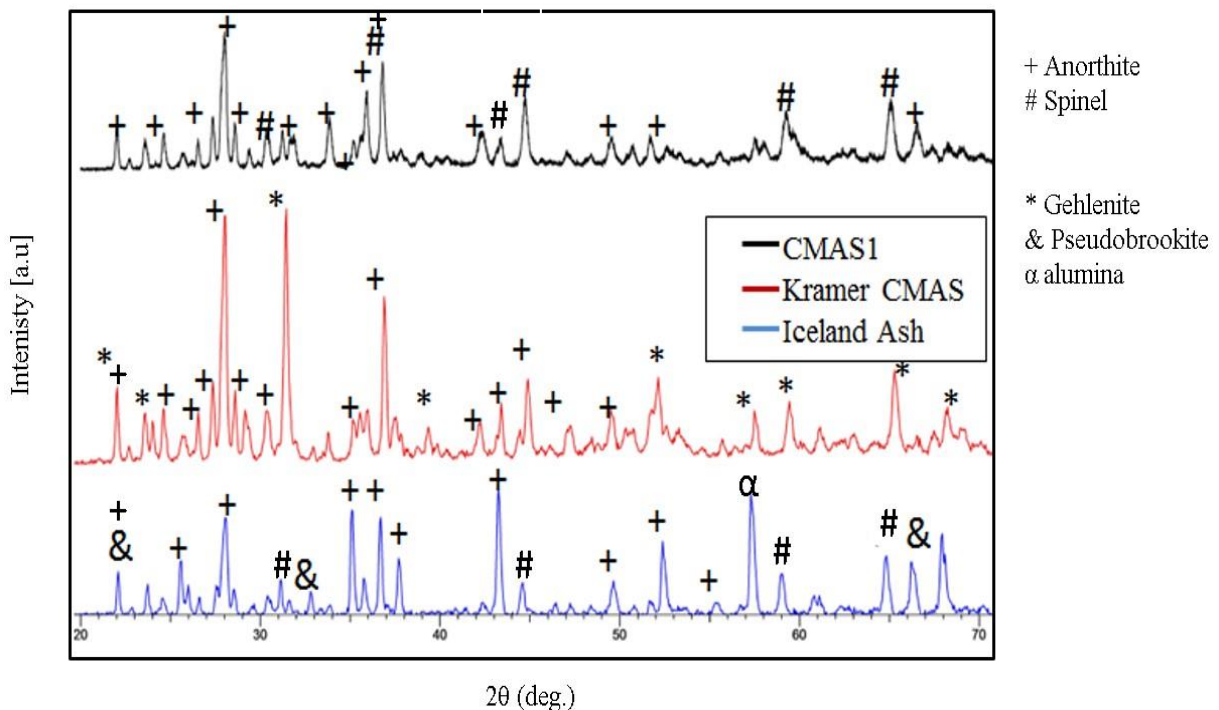


**Figure 4.4:** XRD patterns of CMAS/VA alumina mixtures at 1250°C after 10 h.

## 4.2 CMAS/VA Infiltration tests

### 4.2.1 Short Term Infiltration Tests at 1250°C

Short term infiltration tests for 5 min were conducted on the EB-PVD alumina coatings at 1250°C, in order to categorize the CMAS/VA initial crystallization products. Fig. 4.5 shows the overall SEM cross-sectional view and elemental mapping for all the CMAS/VA infiltrated samples. It can be seen from the image that the CMAS/VA has reacted with Al<sub>2</sub>O<sub>3</sub> and formed a reactive layer at the top of the coating and infiltration in wider gaps. Additionally, the Fig. 4.6 shows high magnification SEM micrographs of the reaction layer which was formed on the alumina layer for all CMAS/VA compositions. The analysis of the reaction layer for all CMAS/VA compositions will be discussed below.

Fig.4.6 (a) shows the SEM cross section image of the reaction zone at CMAS1/EB-PVD Al<sub>2</sub>O<sub>3</sub> interface where the partial sealing of inter-columnar gaps by the dark brown reaction layer identified as spinel (MgAl<sub>1.9</sub>Fe<sub>.1</sub>O<sub>4</sub>) and labeled in the image as # can be observed. Another CMAS crystallizing product, found at the top of spinel, is identified as anorthite and is labelled as +. The light gray colored product at the top of the image and at the center of the columnar gaps represents, the CMAS glass (leftover CMAS) labelled as ^. A total reaction layer thickness of around 2 µm can be seen. The chemical composition of the products was analyzed by means of EDS spot analysis and they were characterized by comparing with the XRD results obtained at 1250°C isothermal heating for 10 hours. Finally, the Table 4.2 provides summary of the chemical composition of the found elements with their respective identified phases.

**Table 4.2** Summary of CMAS1 reaction phases at 1250°C after 5 min. (EDS analysis)

Designation	CMAS Chemical Composition (wt. %)							Phase
	O	Ca	Mg	Al	Si	Fe	Zr	
#	38.50	-	14.00	32.00	-	16	-	Spinel (MgAl <sub>1.9</sub> Fe <sub>.1</sub> O <sub>4</sub> )
+	43.47	16	-	17.44	21.47	-	-	Anorthite (CaAl <sub>2</sub> Si <sub>2</sub> O <sub>8</sub> )
^	36.49	16.41	5.90	7.89	17.03	12.01	-	CMAS Glass

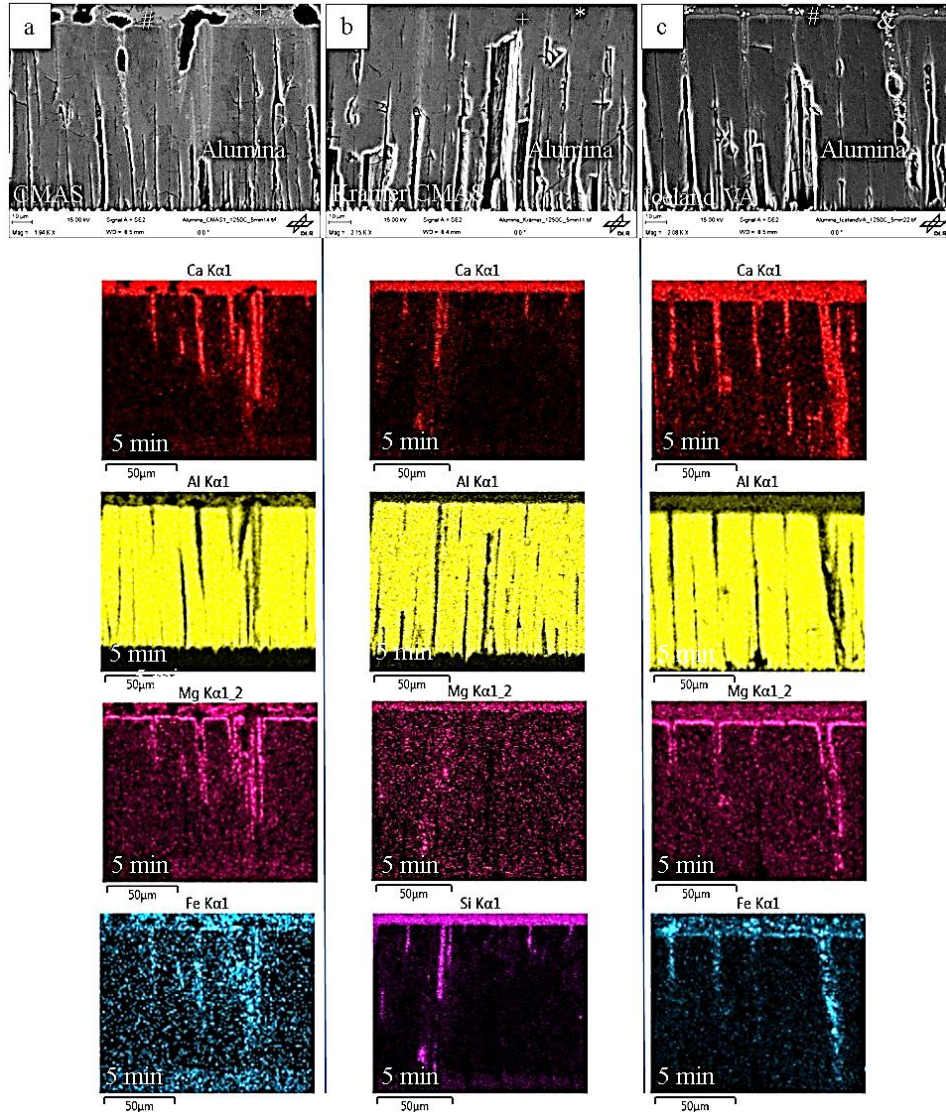


**Figure 4.5:** Short term infiltration tests on EB-PVD alumina with (a) CMAS1, (b) Krämer CMAS and (c) Iceland ash at 1250°C for 5 min.

Fig. 4.6 (b) shows the SEM cross section image of the initial crystallization process of Krämer CMAS/EB-PVDAl<sub>2</sub>O<sub>3</sub> interface. The chemical composition of the products labelled in the image is shown in Table 4.3 with their matching XRD phase obtained from the studies performed in the section 4.1.2.1. The flat crystalline layer growing on the top of alumina is identified as the initial CMAS sealing products i.e., anorthite. In Krämer CMAS, the only CMAS arresting product is identified as anorthite (CaAl<sub>2</sub>Si<sub>2</sub>O<sub>8</sub>) which is labeled as +. The other crystalline product is identified as gehlenite and is labeled as \*. Finally, the dark product layer over the gehlenite is labeled as ^ which represents the glass. A total reaction layer thickness of around 2 μm can be seen.

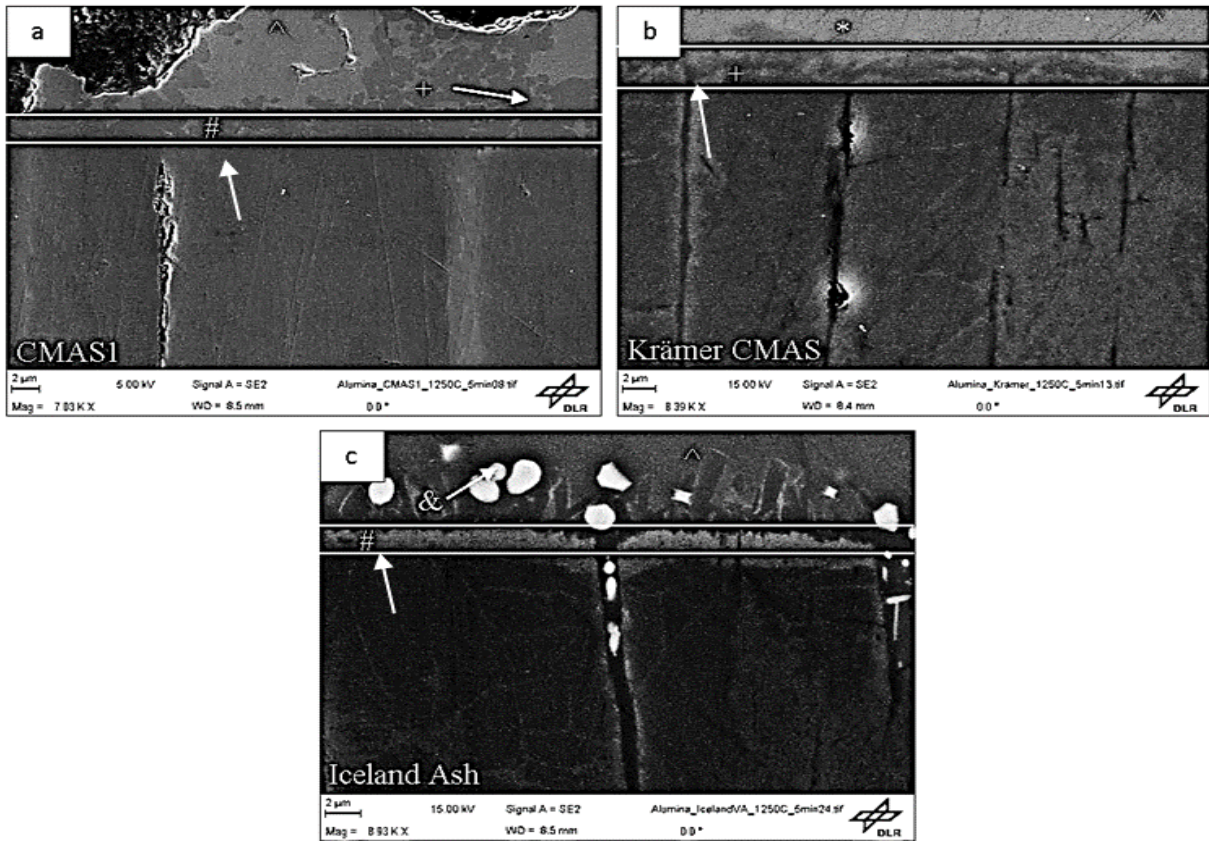


**Figure 4.6:** High magnification SEM micrographs showing the reaction layer for (a) CMAS1, (b) Krämer CMAS and (c) Iceland VA with EB-PVD alumina after 5 min. infiltration at 1250°C.

**Table 4.3** Summary of Krämer CMAS reaction zones at 1250°C after 5 min. (EDS analysis)

Designation	Chemical Composition (wt. %)							Phase
	O	Ca	Mg	Al	Si	Fe	Zr	
+	41.98	11.65	-	29.41	16.96	-	-	Anorthite
*	42.72	17.34	1.23	16.36	22.39	-	-	Gehlenite
^	40.79	23.66	3.77	8.05	23.74	-	-	CMAS Glass

Fig. 4.6 (c) shows the reaction zone of Iceland VA/alumina interface after 5 min. The initial reaction product produced is identified as spinel which was also observed in CMAS1. The spherical crystals containing iron and titanium (pseudobrookite) were formed initially labeled as &, which do not show any sealing property for CMAS crystallization. The EDS spot analysis reveals the high content of iron in pseudobrookite which was already identified in XRD as shown in section 4.1.4. The reaction layer thickness was formed of 2-3  $\mu\text{m}$ . Table 4.4 provides a summary of the phases found along with the respective measured chemical compositions.

**Table 4.4** Summary of Iceland ash reaction zones at 1250°C after 5 min (EDS spot analysis)

Designation	Iceland ash Chemical Composition (wt. %)								Phase
	O	Ca	Mg	Al	Si	Fe	Zr	Ti	
#	36	-	12	33.5	-	18	-	-	Spinel (MgAl <sub>1.9</sub> Fe <sub>.1</sub> O <sub>4</sub> )
&	37	-	-	-	-	56.27	-	6.51	Pseudobrookite
^	43	6.81	2	9.49	26	6.87	-	2.35	Glass

In all studied CMAS/VA/Al<sub>2</sub>O<sub>3</sub> cases, the reaction layer of 2-3 μm thick has formed after 5min at 1250°C. Furthermore, during the heat treatment CMAS/VA completely infiltrated in wider inter-columnar gaps which have occurred because of sintering. For short term thermal exposure, the progression of infiltration was observed only in the wider inter-columnar gaps (i.e., say as vertical direction). However, for longer time of exposure the variation in infiltration kinetics may change. This will be studied in further sections.

## 4.2.2 Long Term Infiltration Tests at 1250°C

The long term isothermal infiltration tests were performed to study the coating infiltration resistance and reaction layer growth over increased periods of time (1 and 10 hours). The total reaction layer is defined as the area from the formation of the spinel phase to the end of unreacted EB-PVD alumina top coat. During the isothermal heat treatment in order to create  $\alpha$ -alumina, heavy sintering of the coatings occurred as a result larger inter-columnar gaps have been formed which lead to no clear description of infiltration depth. Additionally, the reaction layer formed at the CMAS glass/alumina interface is explained in detail for each used CMAS/VA source in the following sections.

### 4.2.2.1 Reaction layer analysis for CMAS1 at 1250°C

The analysis of the reaction layer was performed by categorizing the reaction products using the phases found from the XRD results discussed in section 4.1.4. This analysis will be used to validate the time dependency on reaction products formation and growth of reaction layers.

Fig. 4.7 shows elemental mapping of the reaction layer formed at the CMAS1/EB-PVD  $\text{Al}_2\text{O}_3$  interface showing the main reaction elements after 1 h. and 10 h. of isothermal heating at 1250°C. It can be clearly seen from the elemental mapping that the top layer (#) contains all the available elements which form spinel (Mg, Al and Fe). Another crystallized product on the top of the spinel layer was found and identified as anorthite (+). EDS point analysis was performed on several spots which were shown in Fig. 4.8 and is presented in Table 4.5. The total reaction layer is defined as the area from the formation of the spinel phase to the end of the unreacted alumina top coat. At 1250°C, the total reaction layer measured on top of EB-PVD columns exhibits a uniform thickness of 5  $\mu\text{m}$  and 12  $\mu\text{m}$  for 1 and 10 h respectively. The reaction products did not exhibit a large difference in their chemical composition after 1 h. and 10 h. (Table 4.5). Furthermore, The CMAS1 reaction layer does not show significant changes regarding appearance and formation of new crystalline phases with respect to time. Fig 4.8 shows the high magnification cross sectioned SEM micrographs where the white grid lines indicate the reaction layer at the CMAS1/alumina interphase. The reaction products spinel (#) and anorthite (+) are indicated clearly in the below image. From the elemental mapping it can be clearly seen that the CMAS has completely infiltrated EB-PVD alumina through the wider inter-columnar gaps (vertical direction). However, the infiltration could not proceed through the

circumference of the columns (i.e., horizontally) as the formed spinel layer has assured the sealing of the CMAS.

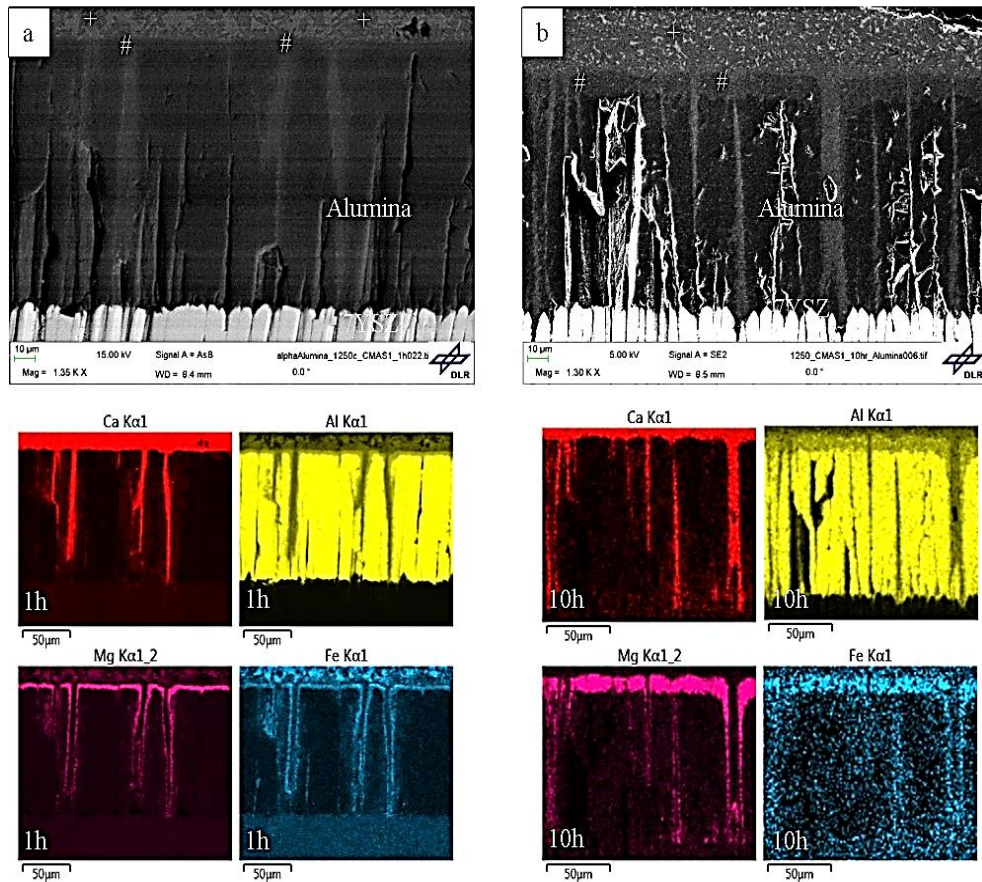


**Figure 4.7:** Elemental mapping of the reaction layer at the CMAS1/alumina interface at 1250°C (a) after 1 h. and (b) after 10 h.

**Table 4.5** Summary of reaction products for CMAS1 after 1 h. and 10 h. at 1250°C.

Time, (h.)	Designation	CMAS Chemical Composition (wt. %)							Phase
		O	Ca	Mg	Al	Si	Fe	Zr	
1 h.	#	41.28	-	14.40	34.90	-	7.50	-	Spinel
1 h.	+	43.16	16	-	17	21.01	-	-	Anorthite
1 h.	^	39.49	17.41	5.30	7.80	17.53	1.52	-	CMAS Glass
10 h.	#	40.10	-	14	36	-	9	-	Spinel
10 h.	+	42.57	15.65	-	18.93	21.61	-	-	Anorthite
10 h.	^	40.78	15.70	1.78	12.89	19.27	8.56	-	CMAS Glass

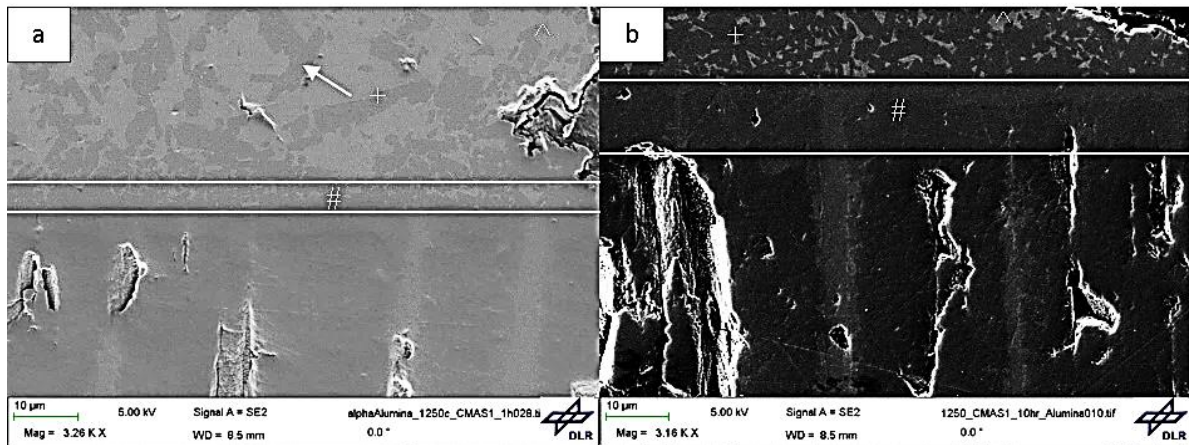


**Figure 4.8:** High magnification image for the reaction layer at the coating/glass interphase for CMAS 1 at 1250°C (a) after 1 h. and (b) after 10 h.

#### 4.2.2.2 Reaction layer analysis for Krämer CMAS at 1250°C

Fig. 4.9 shows the reaction layer formed on top of the Krämer CMAS/EB-PVD alumina interface after 1 h. and 10 h. of isothermal heating at 1250°C. The reaction layer can be identified as anorthite (contains Ca, Al and Si) with the help of elemental mapping shown in Fig. 4.9. The other crystalline product (on top of the anorthite), which doesn't show any arresting properties of CMAS, is identified as gehlenite and labeled as \*. Finally, the bright product layer over the gehlenite which is labeled as ^ (Fig. 4.10) represents the left over CMAS glass. Table 4.6 provides a summary of the reaction products formed with their respective chemical composition. The formed significant reaction products do not have a big difference in the chemical composition.

High magnification SEM micrograph (Fig. 4.10) shows the clear view of reaction products and in between the white lines reaction layer can be observed. After long time exposures, a significant growth of the reaction layer shows an overall uniform thickness of 5 µm and 8 µm after 1 h. and 10 h. respectively.

Coming to the point of Krämer CMAS infiltration, EB-PVD alumina has completely infiltrated. From the elemental mapping, it is observed that the infiltration effect is greater compared to CMAS1 and Iceland VA. This is due to the anorthite between the columns not restricting the CMAS infiltration. Thus the infiltration of CMAS occurs not only in the inter-columnar gaps but also through the circumference of the columns (i.e., in the horizontal direction).

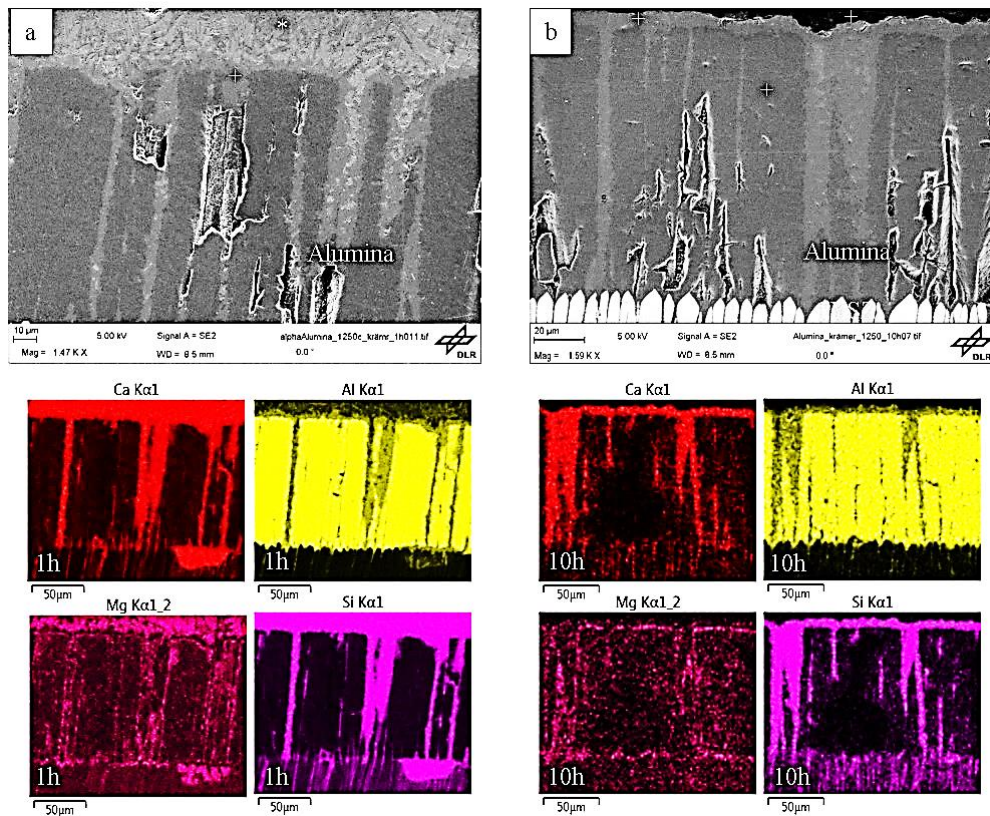


**Figure 4.9:** Elemental mapping of the reaction layer at the Krämer CMAS/alumina interface at 1250°C (a) after 1 h. and (b) after 10 h.

**Table 4.6** Summary of reaction products for Krämer CMAS 1 h. and 10 h. at 1250°C.

Time, (h.)	Designation	Chemical Composition (wt. %)							Phase
		O	Ca	Mg	Al	Si	Fe	Zr	
1 h.	+	44.50	14.66	-	19.13	23.28	-	-	Anorthite
1 h.	*	40.68	28	6	4.8	20.38	-	-	Gehlenite
1 h.	^	42.01	26.66	5.37	6.05	20.74	-	-	CMAS Glass
10 h.	+	45.36	16.95	-	16.81	20.36	-	-	Anorthite
10 h.	*	42.72	25	5	7	24.35	-	-	Gehlenite
10 h.	^	40.79	26.66	5.77	7.05	22.74	-	-	CMAS Glass

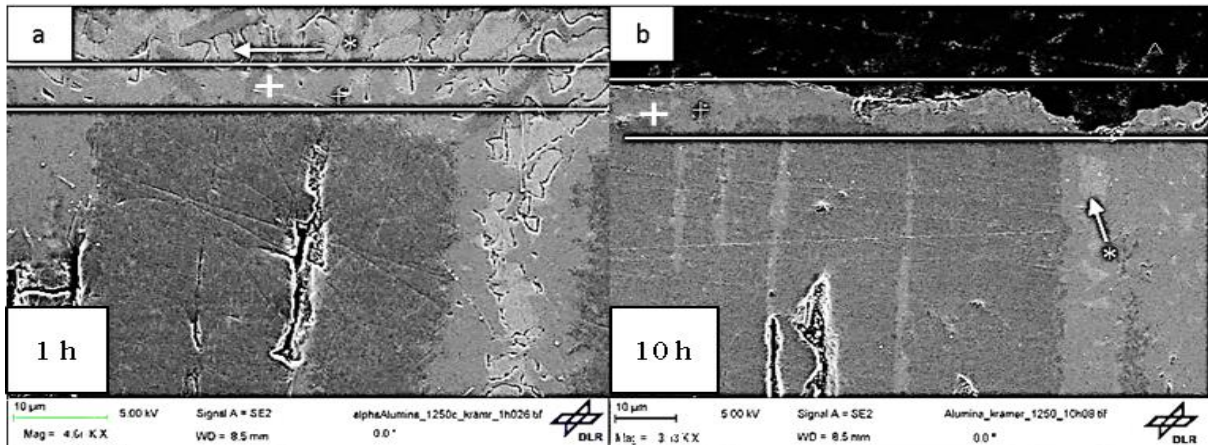


**Figure 4.10:** High magnification image for the reaction layer at the coating/glass interphase for Krämer CMAS at 1250°C (a) after 1 h. and (b) after 10 h.

#### 4.2.2.3 Reaction layer analysis for Iceland ash at 1250°C

Fig. 4.11 shows the reaction layer formed at the VA/EB-PVD alumina interface with the respective elemental mapping showing the main reaction elements for the Iceland ash infiltration after 1 h. and 10 h. of isothermal heating at 1250°C. A flat light brown reaction layer of spinel (Fig. 4.12) is formed on the top of alumina TBC with the enrichment of Mg, Al and Fe which were confirmed by elemental mapping. Spinel (#) reaction layer thickness increased from 3 μm to 7 μm after 1 h. and 10 h. respectively. Also, large pseudobrookite crystals (&) are spotted on the top of spinel layer with high amount of iron and titanium rich contents.

The formation of pseudobrookite is seen when a large amount of glass is available to provide enough Fe and Ti in order to form the large globular iron and titanium rich crystals. With respect to time, the size of iron and titanium crystals increases (see Fig. 4.12). The unreacted glass on top is formed for all the short and long term isothermal tests. The unreacted glass with all CMAS elements flows into the large inter-columnar gaps. Table 4.7 provides a summary of the labeled reaction products with their XRD matched crystal phase. The formed reaction products do not have a big difference in the chemical composition, but the variation in pseudobrookite content was noticed and will be discussed in chapter 5.

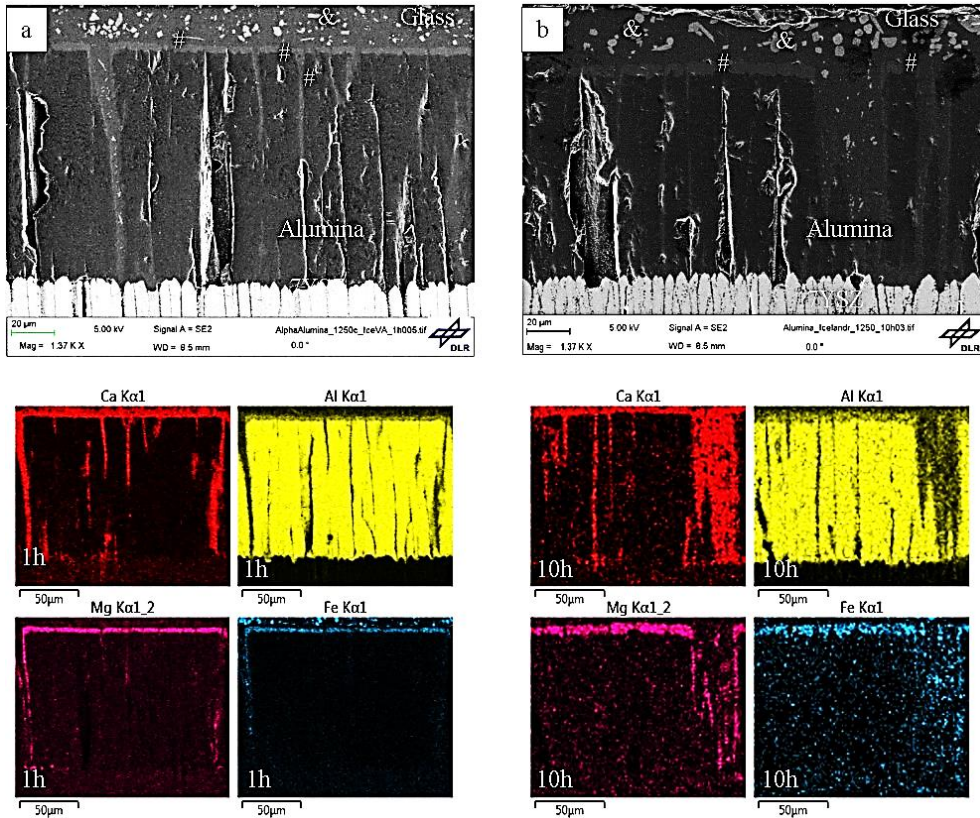


**Figure 4.11:** Elemental mapping of the reaction layer at the Iceland VA/alumina interface at 1250°C (a) after 1 h. and (b) after 10 h.

**Table 4.7** Summary of reaction products for Iceland ash for 1 h. and 10 h. at 1250°C

Time, (h.)	Designation	Iceland ash Chemical Composition (wt. %)								Phase
		O	Ca	Mg	Al	Si	Fe	Zr	Ti	
1 h.	#	39.98	-	10.12	30.65	-	18.49	-	-	Spinel
1 h.	&	35	-	-	-	-	53.27	-	6.01	Pseudobrookite
1 h.	^	46	8.80	2	13.49	25	2.87	-	2.35	Glass
10 h.	#	39.47	-	9.97	30.58	-	18.14	-	-	Spinel
10 h.	&	37	-	-	-	-	40.27	-	24.51	Pseudobrookite
10 h.	^	46.47	7.18	1.65	13	25.2	5.60	-	2.20	Glass

Fig 4.12 shows the high magnification cross sectioned SEM micrographs where the white grid lines indicate the reaction layer at the Iceland VA/alumina interphase. The reaction products

spinel (#) and pseudobrookite (&) are indicated clearly in the below image. From the elemental mapping it can be clearly seen that the Iceland ash has completely infiltrated with in the inter-columnar gaps of EB-PVD alumina. However, it was restricted horizontally (through the circumference of the columns) by the spinel layer between the columns.

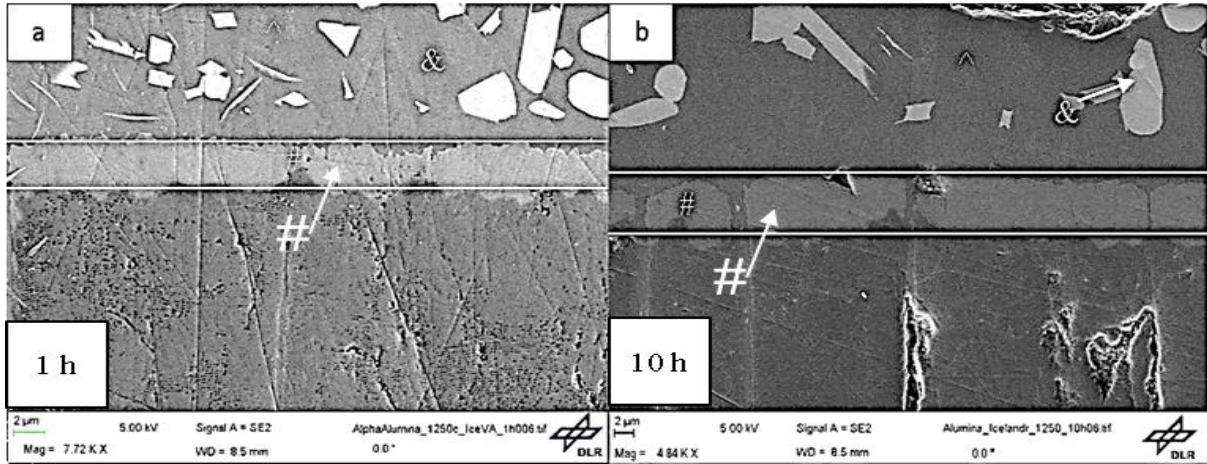


**Figure 4.12:** High magnification image at the Iceland VA/alumina interphase at 1250°C (a) after 1 h. and (b) after 10 h.

The reaction layer growth over time starting from 5 min to 10 h was drawn for all sets of experiments between  $Al_2O_3$  and CMAS/VA and is shown in Fig.4.13.

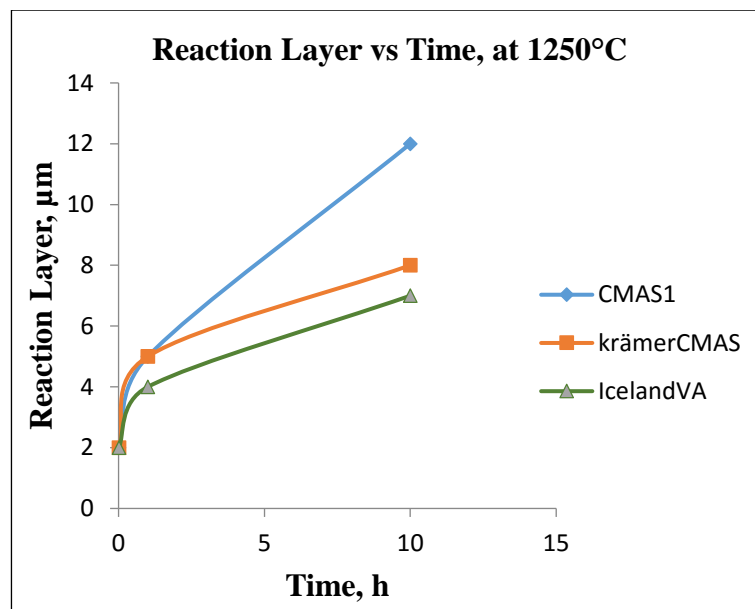


**Figure 4.13:** Progression of reaction layer on top of columns over time for isothermal tests at 1250°C.

For all the used CMAS/VA compositions, there is no big difference in reaction layer growth in between 5 min (2-3 μm) and 1 h (4-5 μm). The largest reaction layer growth after 10 h. is shown

by CMAS1 (12  $\mu\text{m}$ ) followed by Krämer CMAS (8  $\mu\text{m}$ ) and Iceland VA (7  $\mu\text{m}$ ). The reaction layer growth for all CMAS/VA cases was found to be parabolic in nature. The parabolic constants for CMAS1, Krämer CMAS, and Iceland VA were calculated as  $4 \times 10^{-15}$ ,  $1.7 \times 10^{-15}$ , and  $1.7 \times 10^{-15} \text{ m}^2/\text{sec}$ . respectively.

### **4.2.3 Long Term Infiltration Tests at 1225°C**

#### **4.2.3.1 CMAS1 long term infiltration Test at 1225°C**

Fig. 4.14 shows the EDS elemental mapping of the reaction layer formed at the CMAS1/EB-PVD alumina interface after 1 h. and 10 h. of isothermal heating at 1225°C. Two main crystalline phases were observed in EDS Analysis which was identified earlier by XRD analysis (section 4.1.1). The main crystalline phase which blocks the CMAS infiltration is spinel ( $\text{MgAl}_{1.9}\text{Fe}_{0.1}\text{O}_4$ ) was identified on top of EB-PVD alumina column tips. From the high magnification SEM micrograph (Fig. 4.15), the light brown reaction layer on top of alumina with the enrichment of Al, Mg and Fe in the crystallized form was observed. The other formed phase is anorthite (+).

EDS point analysis was performed on several spots which were shown in Fig. 4.15 and is presented in Table 4.8. The total reaction layer is defined as the area from the formation of the spinel phase to the end of unreacted alumina top coat. After long time exposures, a significant growth of reaction layer shows a uniform thickness of 2  $\mu\text{m}$  and 10  $\mu\text{m}$  after 1 h. and 10 h, respectively. Table 4.8 provides a summary of the reaction products formed with their respective chemical composition. The reaction products not exhibited a large difference in their chemical composition after 1 h. and 10 h.

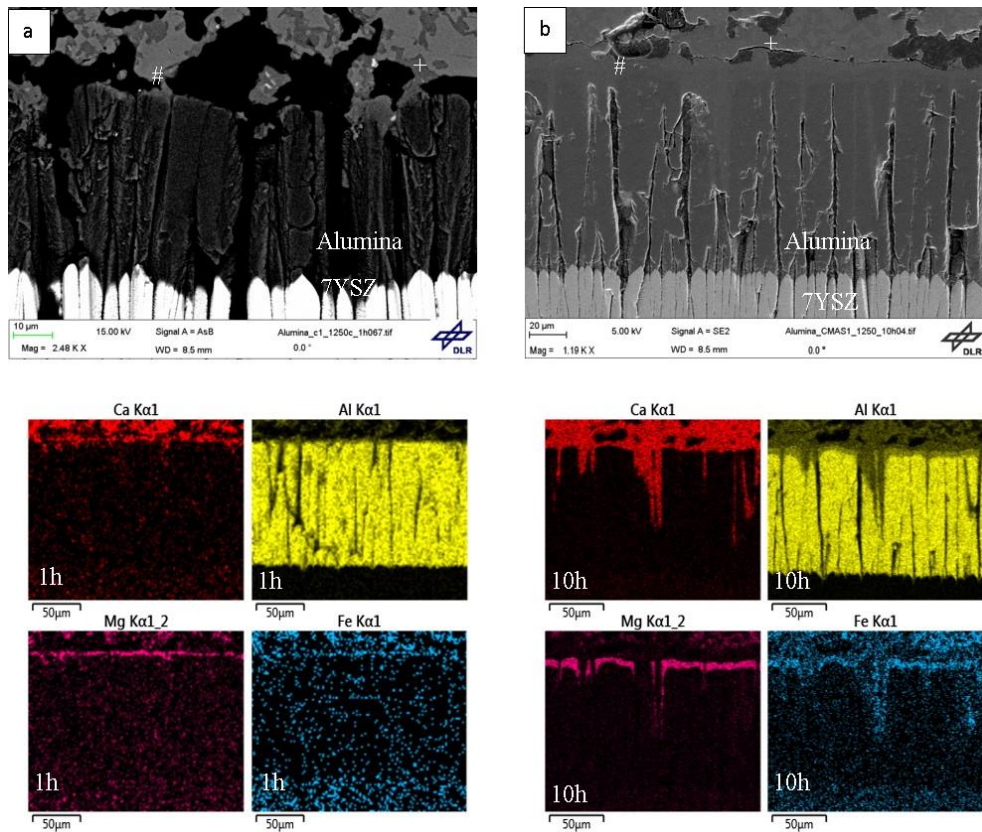


**Figure 4.14:** Elemental mapping of the reaction layer at the CMAS1/alumina interface at 1225°C (a) after 1 h. and (b) after 10 h.

**Table 4.8** Summary of reaction products for CMAS1 1 h. and 10 h. at 1225°C

Time, (h.)	Designation	Chemical Composition (wt. %) after 1 h.							Phase
		O	Ca	Mg	Al	Si	Fe	Ti	
1 h.	#	40.90	-	13.34	36.33	-	8.17	-	Spinel
1 h.	+	43.05	14.20	-	16.91	20.85	-	-	Anorthite
1 h.	^	39.49	17.41	6.90	5.19	20.03	10.01	1.7	CMAS Glass
10 h.	#	41.27	-	13.19	33.61	-	9.60	-	Spinel
10 h.	+	44.05	14.52	-	14.21	20.06	-	-	Anorthite
10 h.	^	41.49	16.23	6.59	5.53	19.26	9.48	1.51	CMAS Glass

Fig 4.15 shows the high magnification cross sectioned SEM micrographs where the white grid lines indicate the reaction layer at the CMAS1/alumina interphase. The reaction products spinel

(#) and anorthite (+) are indicated clearly in the below image. From the elemental mapping it can be clearly seen that the CMAS has 50 % infiltrated (for long time exposure i.e., 10 h.) with in the inter-columnar gaps.

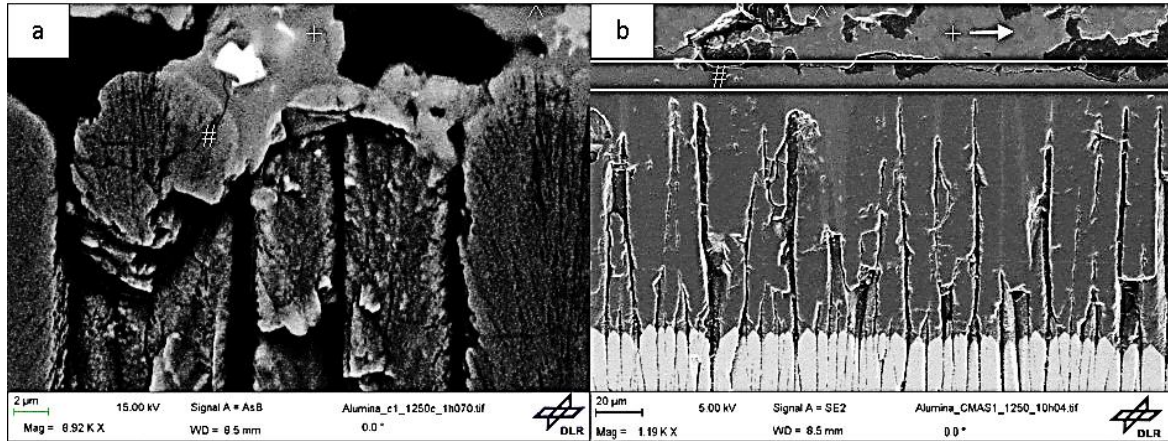


**Figure 4.15:** High magnification image at the alumina/glass interphase at 1225°C (a) after 1 h. and (b) after 10 h.

#### 4.2.3.2 Krämer CMAS long term infiltration Test at 1225°C

It can be seen from the elemental mapping (Fig. 4.16) that the top layer (+) contains all the available elements (Ca, Al, and Si) which forms anorthite. The other crystalline product which doesn't show any sealing properties in infiltration kinetics is identified as gehlenite and labeled as \*. Finally, the dark product layer over the gehlenite, labeled as ^, represents the glass. Table 4.9 provides a summary of the reaction product formed at the Krämer CMAS/alumina interface which does not show any much difference in chemical composition for 1 h. and 10 h. at 1225°C.

Fig. 4.17 shows the high magnification SEM micrographs of the reaction layer at the Krämer CMAS/EB-PVD alumina interface for 1 h. and 10 h. at 1225°C. In that figure, reaction layer can be seen in between the white lines and reaction products can be clearly notified. For long term exposures the growth of the reaction layer thickness is observed (i.e., 7 µm after 10 h). Coming to the point of CMAS infiltration, the Krämer CMAS has not infiltrated significantly at 1225°C. Almost all the CMAS was present on top of alumina even after 10 h.

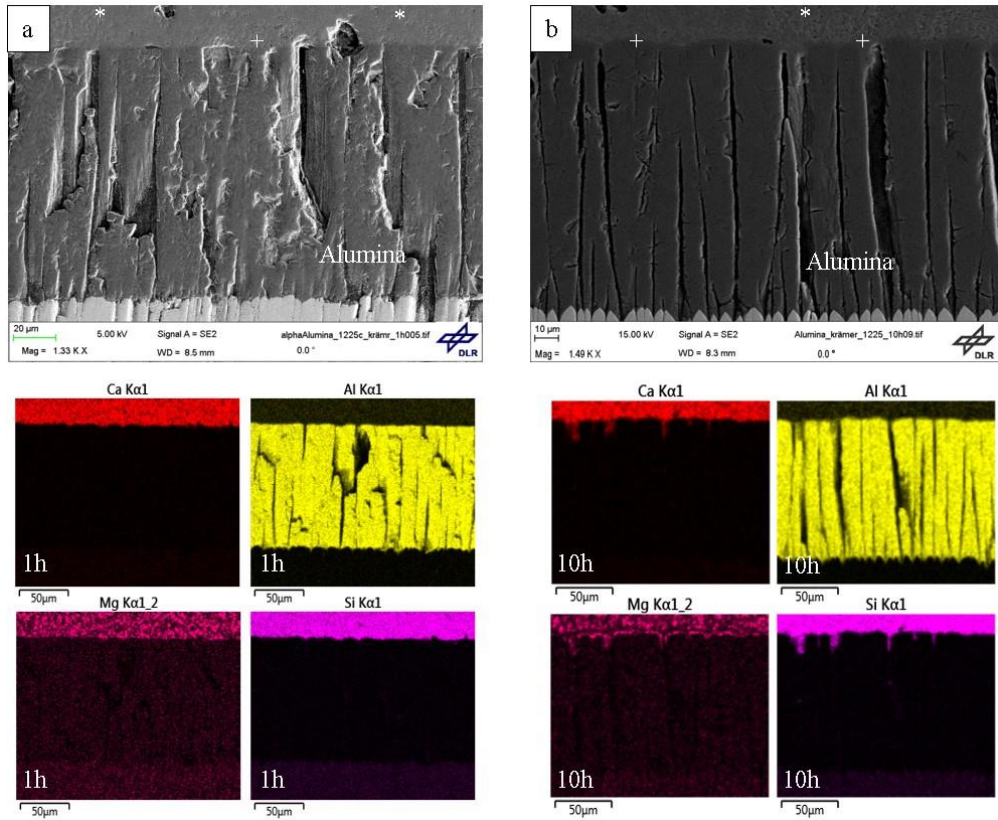


**Figure 4.16:** Elemental mapping of the reaction layer at the Krämer CMAS/alumina interface at 1225°C (a) after 1 h. and (b) after 10 h.

**Table 4.9** Summary of reaction products for Krämer CMAS 1 h. and 10 h. at 1225°C

Time, (h.)	Designation	Chemical Composition (wt. %)							Phase
		O	Ca	Mg	Al	Si	Fe	Zr	
1 h.	+	44	13	-	24	17	-	-	Anorthite
1 h.	*	44.68	18	7.57	5.8	23.36	-	-	Gehlenite
1 h.	^	41.01	26.66	5.37	6.05	21.74	-	-	CMAS Glass
10 h.	+	45.76	14.01	-	20	18.48	-	-	Anorthite
10 h.	*	44	17.65	6.83	6.72	22.56	-	-	Gehlenite
10 h.	^	40.79	25.66	5.77	6.51	22.50	-	-	CMAS Glass

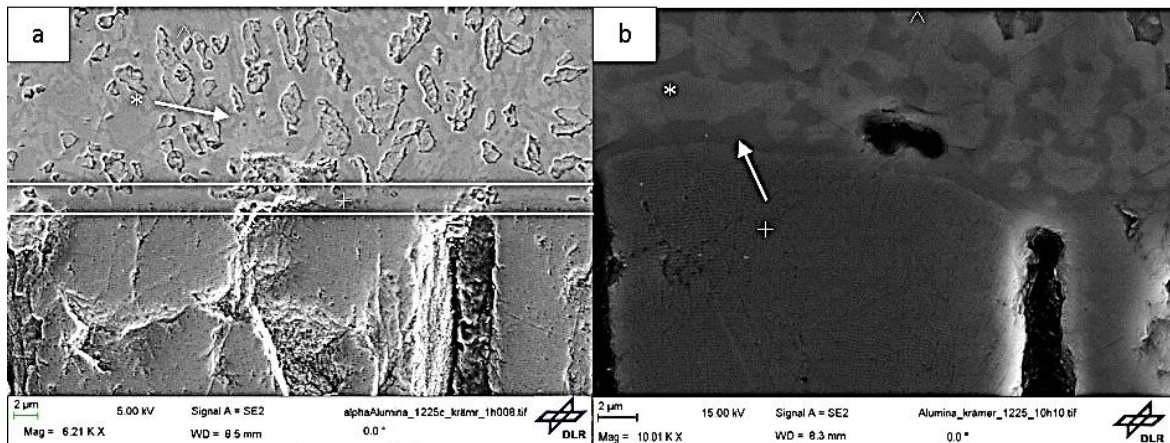


**Figure 4.17:** High magnification image at the Krämer CMAS/glass interphase at 1225°C (a) after 1 h. and (b) after 10 h.

#### 4.2.3.3 Iceland ash long term infiltration Test at 1225°C

Fig. 4.19 shows the high magnification SEM micrographs of the Iceland ash/EB-PVD alumina topcoat interface. The initial reaction produced the main sealing product spinel, labeled as #. The trapezoidal shaped crystals of iron and titanium identified as pseudobrookite were labeled as &, which doesn't show any sealing property for CMAS crystallization. The EDS spot analysis reveals the high content of iron in pseudobrookite which was already identified in XRD shown in section 4.1.4.

Table 4.10 provides a summary of the found phases with their respective measured chemical compositions and has no big change in chemical composition (after 1 h. and 10 h.). The reaction layer formed for the Iceland ash exhibits a similar appearance for 1225°C and 1250°C after 10 h. of thermal exposure. The reaction layer exhibits the same reaction products available for both thermal tests. After long term exposures at 1225°C, a significant growth of reaction layer shows a thickness of 3  $\mu\text{m}$  and 6  $\mu\text{m}$  for 1 h. and 10 h. respectively. The leftover unreacted glass flows through the large inter-columnar gaps. From the elemental mapping it can be clearly seen that the CMAS has completely infiltrated (till the end of alumina top coat) in the vertical direction (see Fig. 4.18). However, the infiltration was restricted horizontally by the spinel layer between the columns.

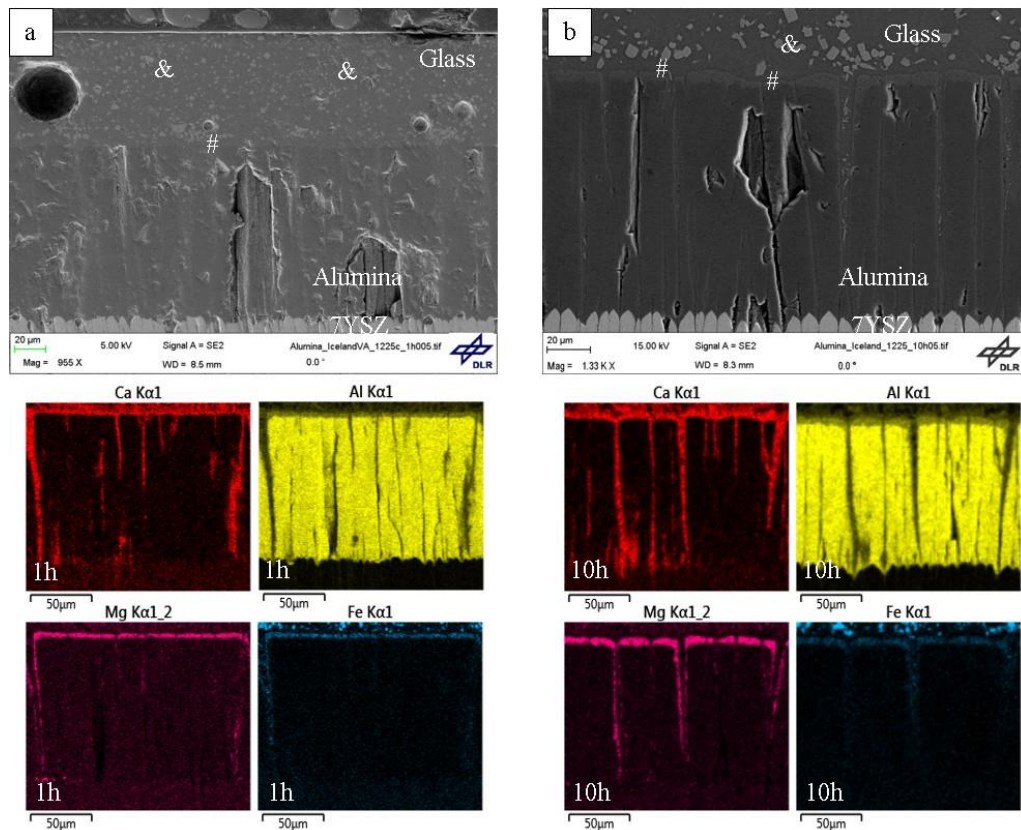


**Figure 4.18:** Elemental mapping of the reaction layer at the Iceland VA/alumina interface at 1225°C (a) after 1 h. and (b) after 10 h.

**Table 4.10** Summary of reaction products for Iceland ash 1 h. and 10 h. at 1225°C

Time, (h.)	Designation	Chemical Composition (wt. %)								Phase
		O	Ca	Mg	Al	Si	Fe	Zr	Ti	
1 h.	#	40	-	12	33	-	15	-	-	Spinel
1 h.	&	28	-	-	-	-	60	-	6	Pseudobrookite
1 h.	^	43	9	2	12	27	4	-	1	Glass
10 h.	#	40.50	-	11.03	31.88	-	14.56	-	-	Spinel
10 h.	&	26	-	-	-	-	61.68	-	6.39	Pseudobrookite
10 h.	^	46.64	8.05	1.02	11.27	26.97	3.48	-	0.60	Glass

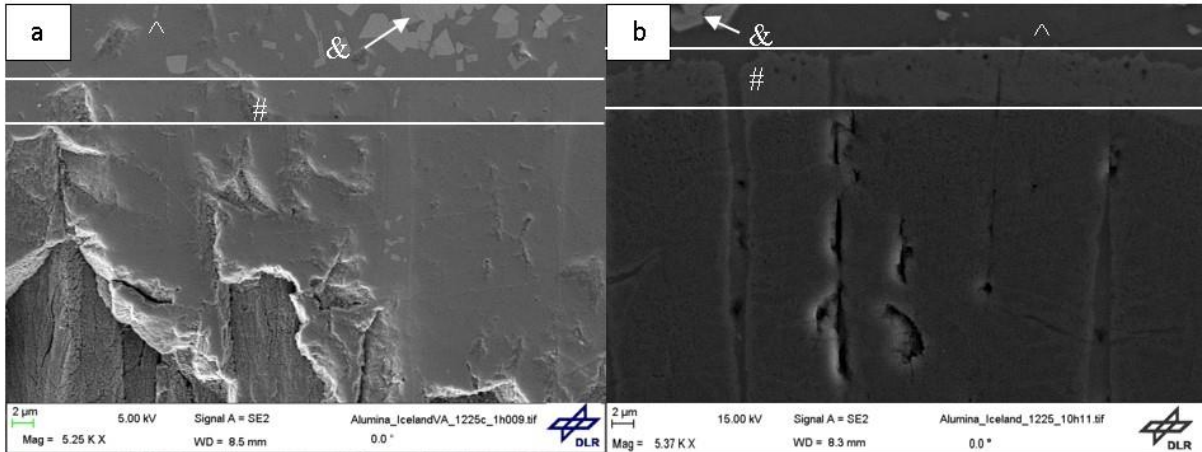


**Figure 4.19:** High magnification image at the alumina/glass interphase for Iceland ash at 1225°C (a) after 1 h. and (b) after 10 h.

The reaction layer growth over time was drawn for all set of experiments between EB-PVD  $\text{Al}_2\text{O}_3$  and CMAS/VA at 1225°C for 1 and 10 h and is shown in Fig. 4.20. The largest reaction layer growth after 10 h. is shown by CMAS1 (10  $\mu\text{m}$ ) followed by Iceland VA (6  $\mu\text{m}$ ) and Krämer CMAS (3  $\mu\text{m}$ ).

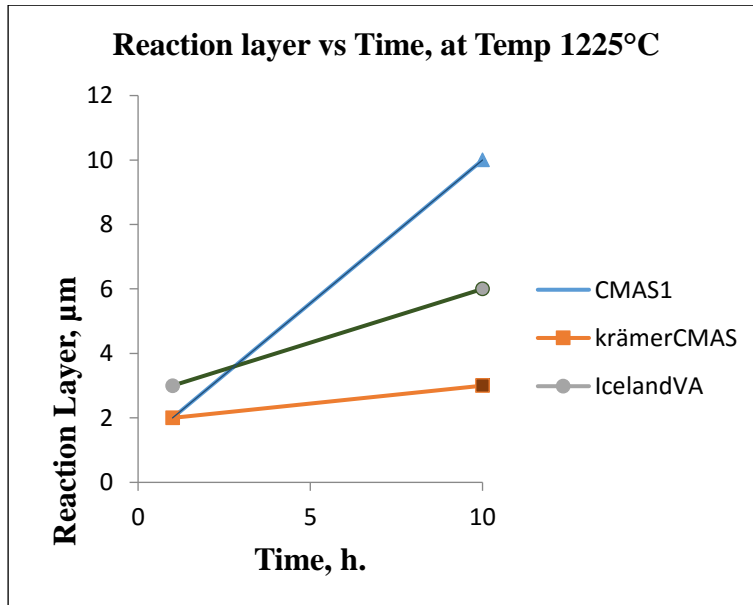


**Figure 4.20:** Progression of reaction layer on top of columns over time for isothermal tests at 1250°C for 1 h. and 10 h.

### **4.3 CMAS Infiltration Tests on RBAO Alumina/7YSZ**

In the previous sections, reaction layers which formed on EB-PVD alumina after short and long term infiltration tests at temperatures 1225°C and 1250°C were extensively studied. However, most of the EB-PVD Al<sub>2</sub>O<sub>3</sub> samples experienced heavy sintering during phase transformation from amorphous alumina to  $\alpha$ -alumina and the formed cracks in the layer have allowed the CMAS/VA to fully infiltrate and hence the infiltration depth (vs) time could not be quantified.

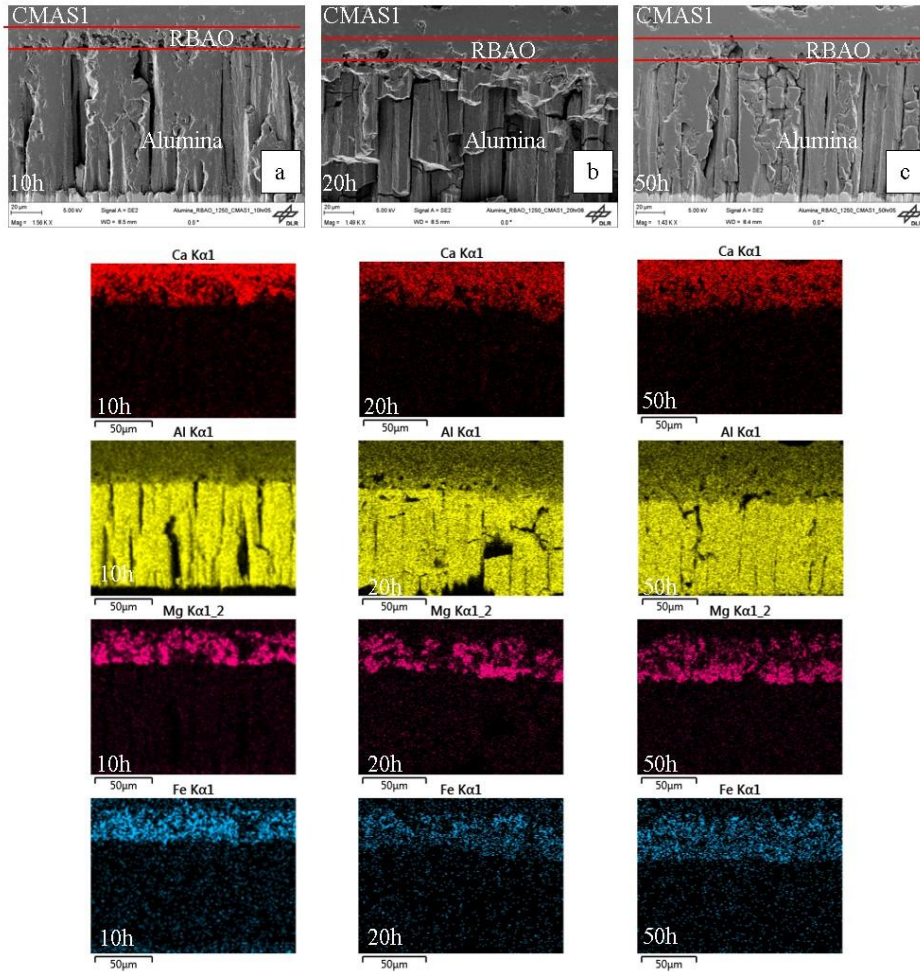
In order to test another alumina microstructure (denser) against long term infiltration tests, RBAO alumina coatings are selected. The RBAO topcoats exhibit excellent adherence and provide a smooth and stable surface. An important benefit of the RBAO process is the oxidation-induced volume expansion of Al, which reduces or even fully compensates sintering related shrinkage and finally prevents coating crack formation [53]. The same circumstance was not achieved by EB-PVD process.

Only CMAS1 has been tested on RBAO Alumina/7YSZ for 10 h, 20 h, and 50 h, at 1250°C. Fig.4.21 shows the corresponding SEM cross-section micrographs and elemental mapping for CMAS1 infiltrated samples. The analysis of the reaction layer for CMAS1 composition with respect to time will be discussed below.

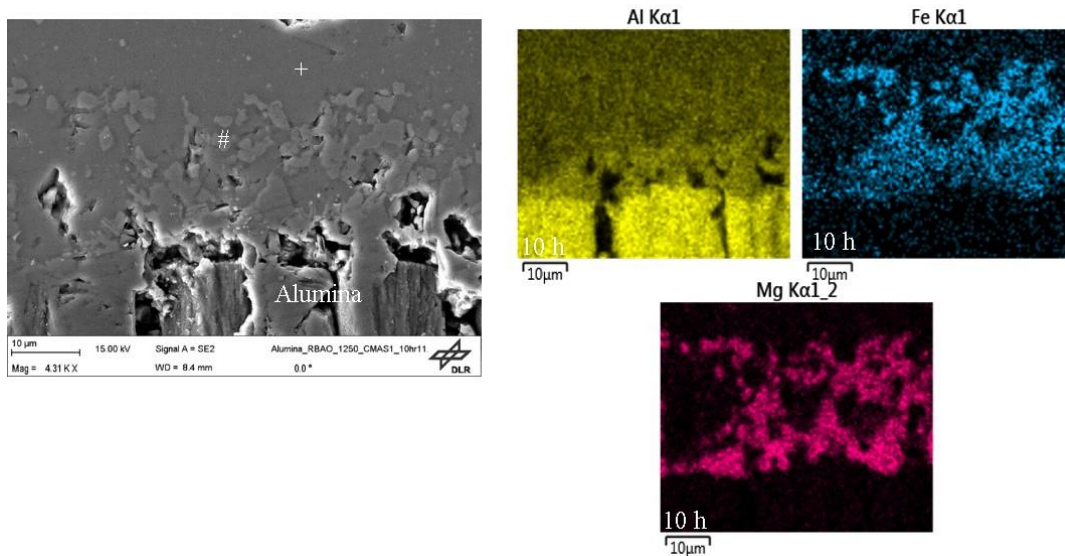
#### **4.3.1 Infiltration Analysis on RBAO topcoat after 10h at 1250°C**

Fig. 4.21 shows the reaction layer formed at the CMAS1/RBAO interface. EDS elemental mapping shows the main reaction elements for CMAS 1 infiltration after 10 h, of isothermal heating at 1250°C. Two crystalline phases were observed in EDS analysis which were identified earlier by XRD analysis (Section 4.1.4). The main crystalline phase which blocks the CMAS infiltration of alumina top coat is spinel (#). The other formed phase is anorthite (+). Additionally, the anorthite crystals do not seem to show any CMAS arresting properties.

It seems that the RBAO (initial thickness 20-25  $\mu$ m) acts as sacrificial layer by consuming all the CMAS and creating a thick sealing layer. Table 4.11 provides the summary of the formed reaction products with their respective chemical compositions. The maximum infiltration depth was around 27  $\mu$ m. After long time exposure for 10 h, reaction layer thickness of 36  $\mu$ m was observed (see Fig. 4.22), whereas the reaction layer thickness of EB-PVD alumina is around 12  $\mu$ m after 10 h.



**Figure 4.21:** CMAS infiltration Tests on RBAO Alumina/7YSZ for 10 h, 20 h, and 50 h.



**Figure 4.22:** EDS mapping for CMAS1/RBAO alumina interface zone at 1250°C after 10 h.

**Table 4.11** Summary of CMAS1 reaction phases at 1250°C after 10 h (EDS analysis)

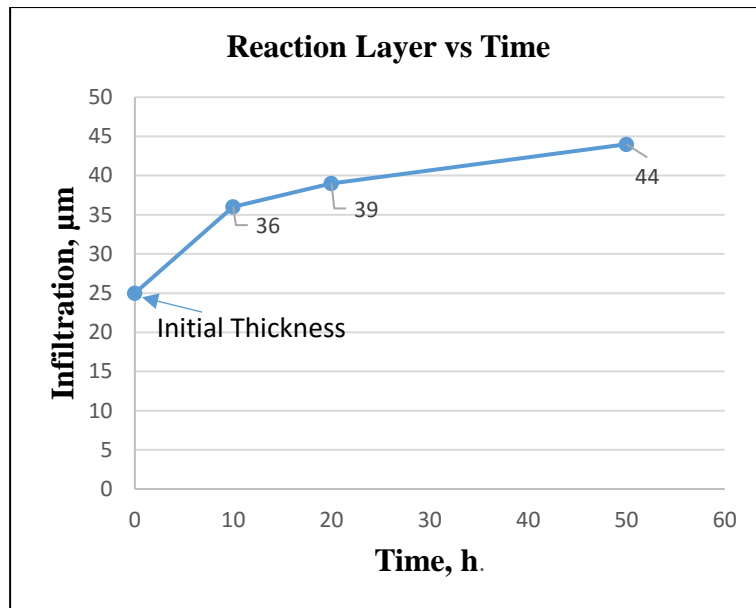
Designation	CMAS Chemical Composition (wt. %)							Phase
	O	Ca	Mg	Al	Si	Fe	Zr	
#	38.21	-	14.90	32.66	-	14.23	-	Spinel ( $MgAl_{1.9}Fe_{.1}O_4$ )
+	42.63	14.90	-	19.10	21.55	-	-	Anorthite ( $CaAl_2Si_2O_8$ )

Table 4.12 shows the summary of the chemical composition for the reaction products after 10 h. and 50 h. for 1250°C at different interfaces. There is no much difference in the chemical composition of spinel (Mg, Al, and Fe) at RBAO/CMAS interface after 10 h. and 50 h. However, at the RBAO/EB-PVD  $Al_2O_3$  interface, there is a variation in the chemical composition of Mg, Al, and Fe compared to RBAO top coat CMAS infiltration. It clearly shows that RBAO consumes all the CMAS and creates a key role in inhibiting further infiltration.

**Table 4.12** Summary of reaction products for CMAS1 at 1250°C for 10 h. and 50 h.

Time, (h.)	Designation	CMAS Chemical Composition (wt. %)							Phase
		O	Ca	Mg	Al	Si	Fe	Zr	
10 h.	# (CMAS1/RBAO)	38.21	-	14.90	32.66	-	14.23	-	Spinel
50 h.	# (CMAS1/RBAO)	38.36	-	13.50	30.32	-	17.83	-	Spinel
10 h.	# (RBAO/ $Al_2O_3$ )	40.73	-	5.29	47.67	-	2.49	-	Spinel
50 h.	# (RBAO/ $Al_2O_3$ )	42.90	-	13.34	36.93	-	7.83	-	Spinel

The total reaction layer exhibits a thickness of 39  $\mu m$  and 44  $\mu m$  after 20 h. and 50 h. respectively. After 50 h., the reaction layer growth is stable. Thereby, it clearly states that the CMAS arresting products formed a thick reaction layer and slowly restricting the further infiltration of CMAS. The reaction layer is growing in a linear way (Fig.4.23). Fig. 4.24 shows the RBAO/EB-PVD alumina interface where initial reaction of EB-PVD alumina with CMAS can be observed and Fe-Mg spinel formation is assured which inhibits the further infiltration.



**Figure 4.23:** Infiltration depth and Reaction layer growth with respect to time for CMAS1/RBAO/Alumina at 1250°C.

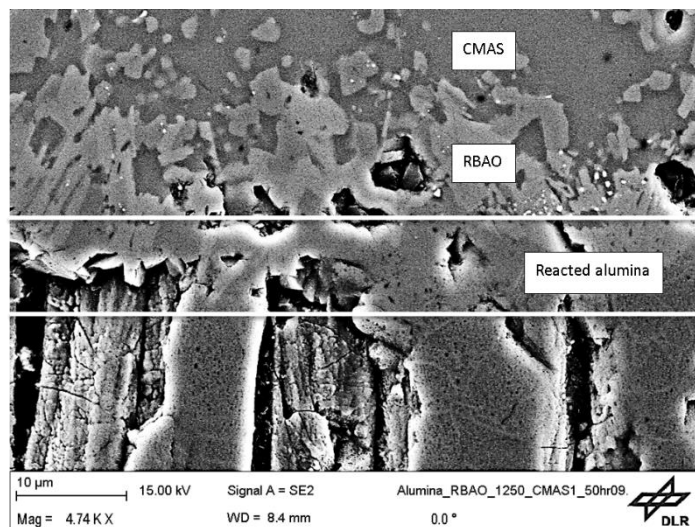


**Figure 4.24:** High magnification SEM micrograph of RBAO/EB-PVD alumina interface at 1250°C after 50 h.

## Chapter 5: Discussion

### 5.1 Manufacturing the EB-PVD alumina top layer on 7YSZ

Differences in the fabricated coatings presented in Fig.4.1 and the corresponding data in Table 4.1 were achieved by varying the process parameters, principally the probe temperature and pressure, while maintaining a constant rotation speed during the EB-PVD deposition process of  $\text{Al}_2\text{O}_3$ . The geometrical characteristics of the created columnar microstructure entirely depend on the process parameters [11, 20, 40]. The substrate temperature is determined by a combination of reflected electrons, vapor condensation, and heat of the melt [8].

Run 1 was characterized by high electron beam energy, resulting in melt spitting and a high substrate temperature (also observed in literature [61]). Due to the high probe temperature ( $890\pm 5$ ) and pressure ( $6\cdot 10^{-3}$  mbar), the coatings obtained after Run 1 were easily spalled and comprised of irregular and asymmetrically distributed primary columns (see Fig.4.1 (a)). Run 2, 3 and 4 were characterized by lower electron beam energy, leading to lower substrate temperature compared to Run 1. Although the substrate temperature was good enough for alumina deposition due to the lower chamber pressure in Run 2, the obtained coatings were also easily spalled and had uniform columnar growth (Fig. 4.1 (b)).

Run 3 was performed by maintaining the sample temperature (as in Run 2) and increasing in the pressure ( $9\cdot 10^{-3}$  mbar). The obtained coatings were of uniform thickness with desired density and columns, but wider inter-columnar gaps were observed (Fig.4.1 (c)). These are formed during evaporation mainly by substrate temperature, secondary shadowing and the angle between the substrate and the plane of vapor incidence [8]. The substrate temperature influences the nucleated primary columns. Therefore, Run 4 was performed by slight increase in sample temperature and a same chamber pressure (as in Run 3). The coatings show regular growth of columns with less inter-columnar gaps and a uniform thickness with desired density (Fig.4.1 (d)). The substrate temperature and chamber pressure had a significant effect on the microstructure of the coatings. However, phase formation of alumina was unaffected during the deposition of the coatings.

$\alpha\text{-Al}_2\text{O}_3$  is the most stable form of the compounds formed between alumina and oxygen [59]. Heat treatment of as-coated alumina coatings (amorphous in nature) was carried out at temperatures above  $900^\circ\text{C}$ , which lead to  $\alpha\text{-Al}_2\text{O}_3$  phase transformation. During the isothermal

heat treatment, heavy sintering occurred between EB-PVD  $\alpha$ -Al<sub>2</sub>O<sub>3</sub> columns, as temperatures exceeding 1100°C [36].

## 5.2 CMAS/VA Infiltration Tests

In the case of EB-PVD Al<sub>2</sub>O<sub>3</sub>/7YSZ coatings, upon CMAS glass infiltration, the dissolution of Al into the glass quickly generates a stable phase that seals the columnar gaps preventing further infiltration [4]. The formed sealing phases at the alumina topcoat/CMAS are spinel (MgAl<sub>1.9</sub>Fe<sub>.1</sub>O<sub>4</sub>), anorthite (CaAl<sub>2</sub>Si<sub>2</sub>O<sub>8</sub>), and other available phases depending on the chemical composition of the melt. A detailed analysis of the reaction layer for the CMAS/VA used will be discussed in the following sections.

### 5.2.1 Reaction Layer Analysis for CMAS 1

Fig. 5.1 shows a schematic of the formed reaction products at the EB-PVD alumina/CMAS1 glass interface. The first and fastest reaction product which grows at the interphase is the spinel (#) which crystallizes the glass in areas such as the alumina topcoat surface, column arms and minor cracks/gaps. This was observed even after 5 min test as shown in section 4.2.1. The spinel layer (contains Mg, Al and Fe) grows by consuming significant amounts of Fe from the CMAS glass. For CMAS 1, the spinel is the most stable phase present in the reaction layer, which grows with respect to time starting from initial thickness of 2  $\mu$ m (5 min.) and grows to 12  $\mu$ m after 10 h at 1250°C. The constant growth of the spinel phase is believed to be due to the presence of Mg and Fe in the CMAS1. After the spinel formation, left over Ca and Si react with CMAS and form a stable anorthite phase (+) on top of the spinel which is shown in Fig. 5.1. CMAS was found to crystallize into anorthite and spinel by chemically interacting with  $\alpha$ -alumina reported in literature was confirmed in this work [39]. The anorthite phase is known for its stability which was reported to generate sealing properties [37, 39]. However, in this reaction the anorthite phase is only found on top of the reaction layer as a sub-reaction product without sealing capability since a large reservoir of glass is available.

Table 4.2 and Table 4.5 provide a summary of the chemical composition of the reaction products that are formed after 5 min. and 10 h. at 1250°C in order to compare the changes in chemical composition with respect to time. It is clear from the chemical analysis that the composition of the reaction products does not have a significant variation with respect to time which states that the reaction is stable after long thermal exposure.

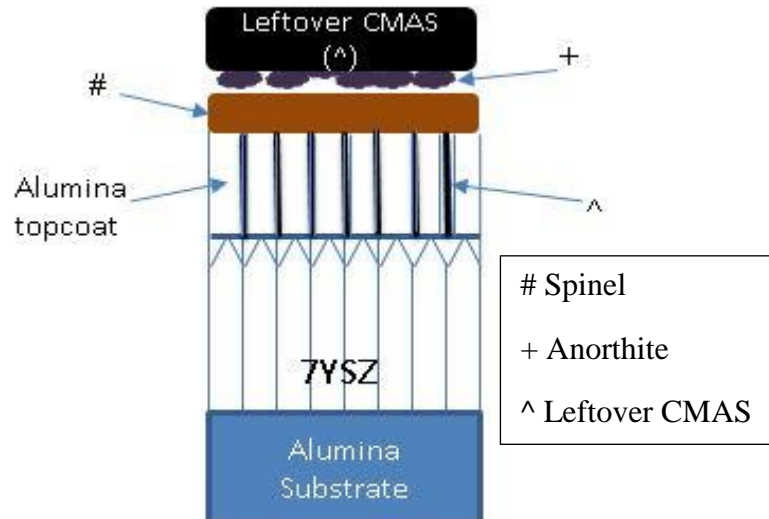


**Figure 5.1:** Schematic reaction layer for CMAS 1 at 1250°C.

The reduction of Fe content in the glass after 10 h shows, its consumption for the growth of spinel phase formation. EB-PVD  $\text{Al}_2\text{O}_3$  coatings exhibited cracks and gaps between the facets (surface and columns) act as a reduced barrier for the penetration of the CMAS melt [62]. From the elemental mapping (Fig. 4.7) it can be clearly seen that CMAS1 has completely infiltrated with in the wider inter-columnar gaps. However, it was restricted through the circumference of the columns by the spinel layer between the cracks that are present as a result of sintering.

### 5.2.2 Reaction Layer Analysis for Krämer CMAS

Fig. 5.2 shows the schematic representation of the reaction layer interphase between alumina/Krämer CMAS at 1250°C. The first reaction product formed on top of the alumina layer was anorthite (+) with the enrichment of Ca, Al and Si which was shown after 5 min. infiltration test in the section 4.2.1. The anorthite represents a stable phase which is reported to generate sealing properties of CMAS [37, 39]. However, the anorthite phase is found as a reaction product without any sealing capability. This might have formed during the cooling phase of the CMAS or it might have formed too slowly rather than as a reaction product. Since a large reservoir of glass is available the anorthite layer grows by consuming the Ca and Si content from the glass (long time exposure, 10 h.). The other crystalline product, which doesn't show any sealing properties of CMAS, is identified as gehlenite (\*). It has formed on top of anorthite. Table 4.3 and Table 4.6 show the summary of chemical composition of the formed reaction products after 5 min. and 10 h. at 1250°C. It can be seen from the table that the chemical composition of the reaction products does not have any significant change with respect to time (after long time exposure).

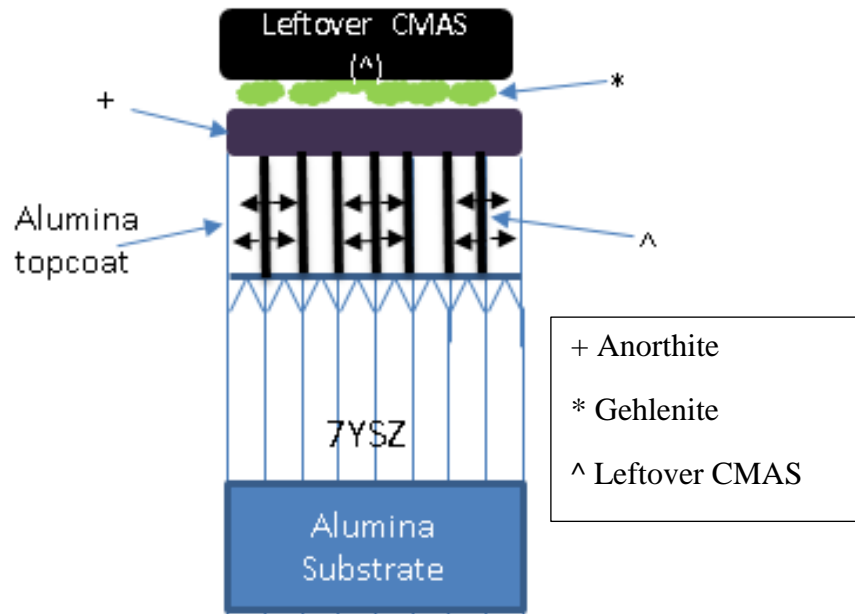


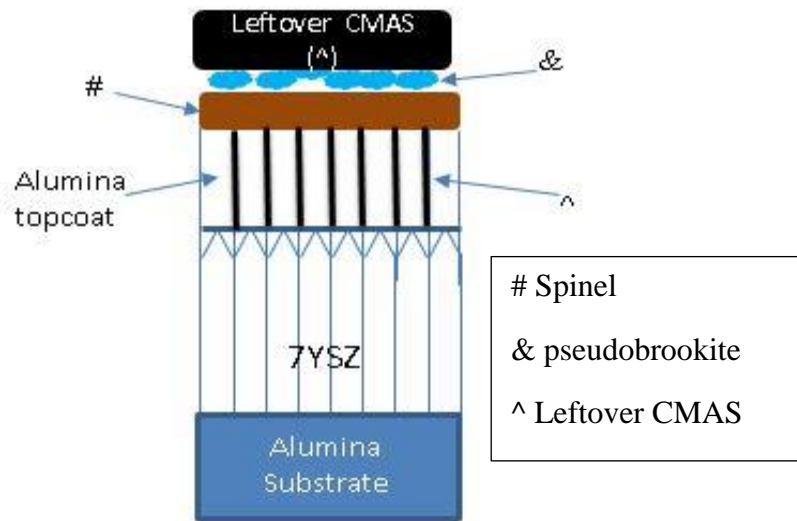
**Figure 5.2:** Schematic reaction layer for Krämer CMAS 1 at 1250°C.

From the gained knowledge, it was seen that Fe is a key element which crystalizes the spinel phase [56]. Lack of Fe content in the Krämer CMAS, formation of spinel layer did not occur. Due to this, the effect of infiltration is more dominant in Krämer CMAS (See Fig. 4.9), which has completely infiltrated. Cracks were observed in the protective material coatings (EB-PVD alumina) because of sintering at high temperatures which provide an easy path for CMAS penetration [62]. Due to the wider gaps and also with the inability of anorthite phase in restricting the CMAS flow, the infiltration with in the wider inter-columnar gaps (cracks) and also through the circumference of the columns (i.e., leakage in to the columns see Fig. 5.2) occurred.

### 5.2.3 Reaction Layer Analysis for Iceland VA

Fig. 5.3 shows the schematic of reaction products formation of alumina/molten VA interphase of Iceland VA at 1250°C. In this case, the reaction is also started by the formation of spinel layer generating the initial sealing of the molten glass as shown in the section 4.2.1 [37, 39]. The growth of the spinel layer (Mg, Al and Fe) in thickness is very slow (section 4.2.2), when compared to CMAS1 as most of the Fe content in Iceland VA was consumed by the pseudobrookite (&). The Fe content in Iceland VA is double the amount in CMAS1 and it has been crystalized into two different products (i.e., spinel and pseudobrookite). As more Fe content is available for the reaction, the accumulation of Fe and Ti leads to the formation of the pseudobrookite (&) crystals. For long time exposure, the accumulation of pseudobrookite crystal

size increases due to the constant diffusion of Fe and Ti (section 4.2.3.3). The mentioned pseudobrookite particles (&) are not believed to have a significance in sealing of the TBC.



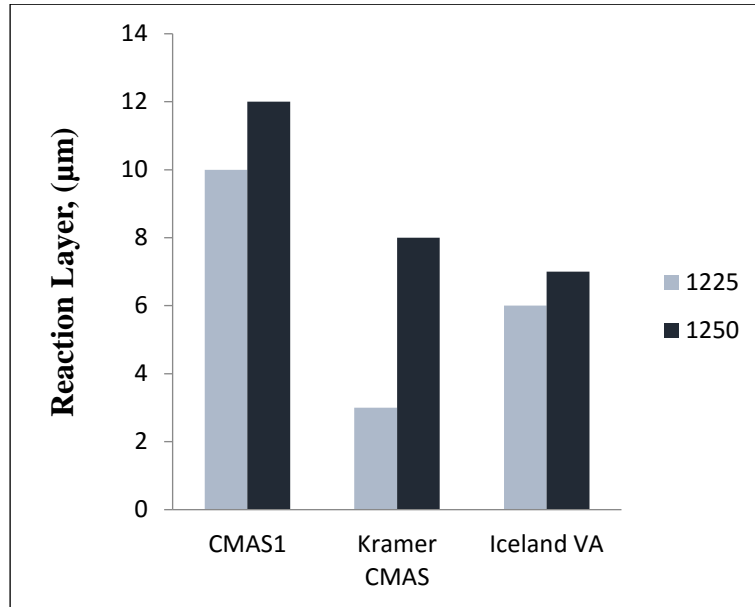
**Figure 5.3:** Schematic reaction layer for Iceland VA at 1250°C

Table 4.4 and Table 4.7 show the summary of the chemical composition for the reaction products after 5 min. and 10 h. for 1250°C. The tables exhibit a minimal change in the chemical composition with respect to time for the reaction products identified in the reaction layer interphase. In general, the pseudobrookite reaction product exhibits the most noticeable change in its chemical composition compared to the other products. It exhibits an increase in Ti and a decrease in Fe content, where the Fe content from glass acts as a sink for stabilizing spinel layer on top. EB-PVD Al<sub>2</sub>O<sub>3</sub> coatings (thickness of 8 μm) exhibited cracks and gaps (because of sintering) act as a reduced barrier for the penetration of the CMAS melt [62]. From the elemental mapping (Fig 4.11 and Fig. 4.18) it can be clearly seen that the CMAS has completely infiltrated (at 1225°C and 1250°C) with in the larger inter-columnar gaps (cracks). However, it was restricted leakage in to the columns by the spinel layer between the columns.

#### 5.2.4 Reaction layer Growth and Temperature Dependency

Fig. 5.4 shows the reaction layer growth for CMAS/VA after 10 h. infiltration at 1225°C and 1250°C. The largest thickness of the reaction layer is shown by CMAS1 followed by Krämer CMAS and Iceland VA at 1250°C. In the case of CMAS1 the large increase in reaction layer growth was due to the formation of main crystallization product (spinel) and it may be that the growth of spinel is faster than anorthite. Krämer CMAS has very thin reaction layer at 1225°C and the reason can be the very slow reaction progression of anorthite at this temperature. The

reaction layer of Krämer CMAS increases at 1250°C and it might be the same anorthite reaction is faster at this temperature. The reaction layer growth of Iceland VA is less compared to CMAS1 because of the large Fe content in Iceland VA (relative to CMAS1) leads to formation of two Fe rich products i.e., spinel and pseudobrookite. Thus, most of the Fe content is consumed by pseudobrookite crystals, resulting in the smaller reaction layer.



**Figure 5.4:** Reaction layer growth on EB-PVD alumina column tips for CMAS/VA after 10 h. infiltration for 1225°C and 1250°C.

The formed reaction products were similar at temperatures 1225°C and 1250°C after reaction of alumina with CMAS/VA compositions. At 1225°C, infiltration depth of CMAS1 and Krämer CMAS is approximately 50% and 8% respectively. The infiltration depth of CMAS1 was low as it starts melting partially at 1225°C [15]. Coming to Krämer CMAS the infiltration depth was found even low as it starts melting at 1235°C [56]. The infiltration of Iceland VA was same at 1225°C and 1250°C. As the Iceland VA melts at 1150°C, there is enough time for the VA to be in liquid state to infiltrate and has resulted with complete infiltration. All CMAS/VA were completely infiltrated at 1250°C as all CMAS/VA were completely molten at 1250°C (Fig. 5.5).

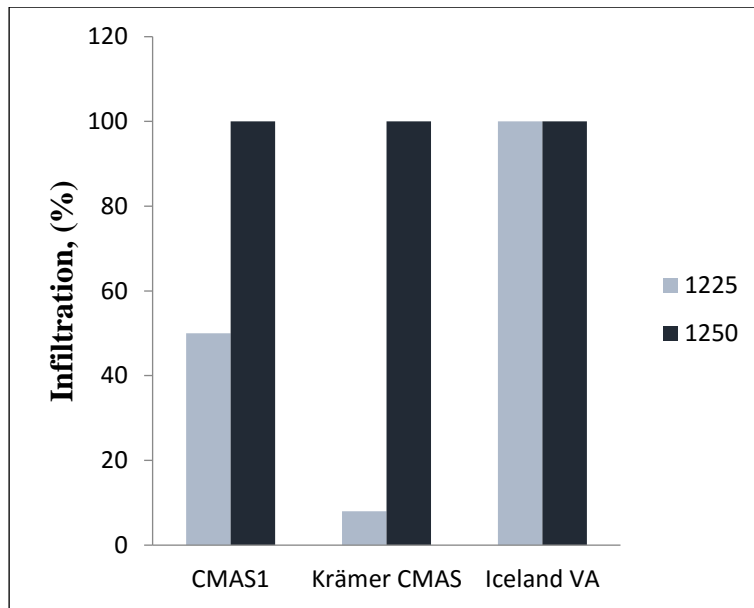


**Figure 5.5:** Infiltration depth within the inter-columnar gaps of EB-PVD alumina vs Time for CMAS/VA after 10 h. infiltration after 1225°C and 1250°C.

### 5.3 Infiltration Analysis on RBAO Alumina top coat

Even though EB-PVD alumina reacted quickly with CMAS/VA compositions and formed stable CMAS sealing products, wider inter-columnar gaps formed due to the heavy sintering of EB-PVD alumina [62]. As soon as CMAS/VA melts, it uses these gaps to infiltrate immediately as shown in short term infiltration tests. RBAO was applied on top of EB-PVD alumina as a sacrificial layer to form a thick layer of CMAS sealing products and help in restricting the further infiltration.

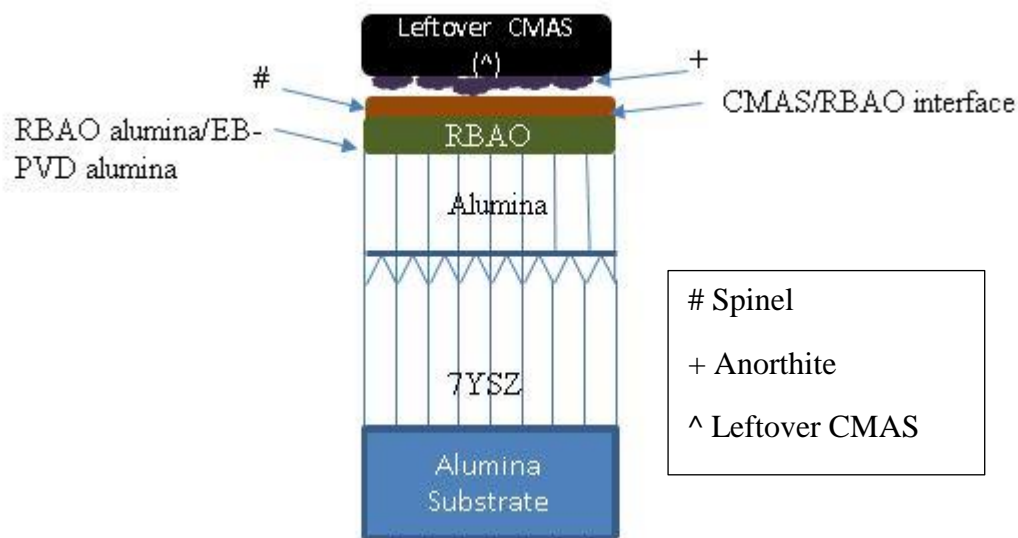


**Figure 5.6:** Schematic Reaction layer for RBAO CMAS1 at 1250°C for 10 h.

The infiltration behavior as well as reaction layer growth of RBAO alumina coating was tested for different time intervals of 10 h, 20 h, and 50 h (only for CMAS1). Fig. 5.6 shows the schematic of reaction product formation at the RBAO/molten glass interface of CMAS1 at 1250°C. RBAO reacts with CMAS and forms the same CMAS arresting products as in EB-PVD alumina top coat. The formed reaction products, such as spinel (#) and anorthite (+), crystallize the glass at the RBAO surface. The formed spinel is the most stable phase present in the reaction layer [37, 39]. Its thickness was measured as 36 μm (after 10 h.) and increased to 39 μm and 44 μm after 20 h and 50 h, respectively. The only difference in the EB-PVD to RBAO alumina coatings is the porosity network which might have played a different role on reducing the sintering cracks of EB-PVD alumina layer. Hence most of the RBAO coating was infiltrated initially but by that time it has also reacted with CMAS and formed the spinel. On the top of spinel, anorthite phase (+) is found as a sub-reaction product without any sealing capability.

Table 4.12 shows the summary of the chemical composition for the reaction products after 10 h. and 50 h. for 1250°C. There is no much difference in the chemical composition of spinel (Mg, Al, and Fe) at RBAO/CMAS interface after 10 h. and 50 h. However, at the RBAO/EB-PVD Al<sub>2</sub>O<sub>3</sub> interface, there is a variation in the chemical composition of Mg, Al, and Fe compared to RBAO top coat CMAS infiltration. It clearly shows that RBAO consumes all the CMAS and plays a key role in inhibiting further infiltration. From the literature it is known that the most efficient TBC coating in arresting CMAS was Gd-zirconate and it has formed a reaction layer of 30 μm when it is subjected to a heat treatment for 4 h at 1300°C [55]. In comparison, a maximum infiltration depth of 41 μm was observed after 50 h at 1250°C in RBAO/EB-PVD alumina against CMAS in this study. It clearly states that the RBAO alumina is probably another reliable candidate material for CMAS mitigation.

## Chapter 6: Conclusion

This work demonstrates the fabrication of EB-PVD alumina/7YSZ coatings as CMAS/VA resistant coatings and the formed CMAS arresting products play a key role in inhibiting further infiltration of CMAS.

EB-PVD Al<sub>2</sub>O<sub>3</sub>/7YSZ TBCs were fabricated by varying the process parameters, especially the substrate temperature, chamber pressure, and rotation speed. By varying the mentioned parameters significant differences in the morphology (i.e., shape, column growth density, and inter-columnar gaps) were noticed. Based on the parameter study the best microstructure characterized by uniform columns with less inter-columnar gaps was chosen for the CMAS/VA infiltration experiments. As the coated alumina has resulted in metastable alumina layer an additional heat treatment was done at 1100°C to transform this metastable to a stable alpha alumina layer.

EB-PVD Al<sub>2</sub>O<sub>3</sub>/7YSZ TBCs were tested on lab scale under CMAS/VA infiltration for short term (5 min.) and long term infiltration (1-10 h.) in the temperature range from 1225 to 1250°C. The alumina coatings exhibited a CMAS/VA resistance by forming CMAS arresting products. The formed stable reaction products (i.e., spinel (MgAl<sub>1.9</sub>Fe<sub>0.1</sub>O<sub>4</sub>) and anorthite (CaAl<sub>2</sub>Si<sub>2</sub>O<sub>8</sub>)) have sealed the smaller gaps against infiltration and generated a uniform reaction layer at the TBC/molten glass interphase which exhibited a minimal growth with time. The formation of spinel and anorthite on crystallization of molten glass previously reported in literature was confirmed in this work. The infiltration could not be prevented or sealed in the larger cracks that are formed due to the high temperature sintering as a by-product of infiltration and pre-heat treatment processes. However, the alumina coatings exhibited good reaction with CMAS/VA and quickly formed CMAS sealing products.

The Fe content in CMAS/VA plays a significant role in forming sealing products of CMAS/VA. In the case of CMAS1 and Iceland VA which contain high amounts of Fe, the diffusion of Al into the Fe rich glass exhibits a higher activity in generating the CMAS sealing product i.e., spinel (enrichment of Mg, Al and Fe). The stable growth of the spinel layer at the CMAS/alumina interface after long term infiltration (at temperatures 1225°C and 1250°C) was observed. Additionally, the high presence of Ca in Krämer CMAS is believed to have a major

influence on the reaction layer growth by stabilizing the anorthite phase on top. A lack of Fe content in Krämer CMAS prevented the formation of spinel. For all the CMAS/VA compositions, reaction layer progresses slowly with respect to time. The effect of infiltration depth is more dominant in Krämer CMAS compared to CMAS1 and Iceland VA with respect to the EB-PVD alumina coatings.

However, the microstructure of the coatings needs to be modified for improved performance since at localized areas where large columnar gaps were available, the CMAS has infiltrated deeply into the coating. In order to seal this wider inter-columnar gaps multifunctional reaction bonded alumina coatings were fabricated on top of crystallization annealed EB-PVD alumina. The deposited RBAO alumina layer has showed a desired porosity network after necessary heat treatment. During infiltration tests, CMAS has reacted with the RBAO coating forming the CMAS crystallization products. The maximum infiltration depth of 41  $\mu\text{m}$  after 50 h. states that the new microstructure has succeeded in preventing CMAS infiltration by forming same crystalline products. Thereby, a phenomenal CMAS resisting top coat on thermal barrier coating was developed. An assessment on the spallation behavior of the reaction layer has to be tested under thermal cycling tests and mechanical stability of the reaction layer has to be determined which can be done in future.

## Bibliography

- [1] David R. Clarke, Matthias Oechsner, Nitin P. Padture, „Thermal barrier coatings for more efficient gas-turbine engines,“ *Materials Research Society*, Bd. 37, pp. 891-898, 2012.
- [2] A. Flores Renteria, B. Saruhan, U. Schulz, H.J. Raetzer Scheibe, J. Haug, A. Wiedenmann, „Effect of morphology on thermal conductivity of EB-PVD PYSZ TBCs,“ *Surface and Coating Technology*, Bd. 201, pp. 2611 - 2620, 2006.
- [3] Alessandro Armellini, Luca Casarsa, Claudio Mucignat, „Experimental assessment of the aero-thermal performance of rib roughened trailing edge cooling channels for gas turbine blades,“ *Applied Thermal Engineering*, Bd. 58, pp. 455-464, 2013.
- [4] Zhang Xiao-feng, Jin-bing, Min, liu, „In situ synthesis of alpha alumina layer on the thermal barrier coating for protection against CMAS (CaO-MgO-Al<sub>2</sub>O<sub>3</sub>-SiO<sub>2</sub>) corrosion.,“ *Surface and Coating Technology*, Bd. 261, pp. 54-59, 2015.
- [5] Sanjay Sampath, Uwe Schulz, Maria Ophelia Jarligo, and Seji Kuroda, „Processing science of advanced thermal barrier systems,“ *Materials Research Society*, Bd. 37, pp. 903-910, 2012.
- [6] J. R. Nicholls, K. J. Lawson, A. Johnstone, D. S. Rickerbt, „ Low Thermal Conductivity EB-PVD Thermal Barrier Coatings,“ Bde. %1 von %2369-372, pp. 595-606, 2001.
- [7] Kendra M. Grant, Stephan Krämer, Jan P.A. Löfvander, Levi, „CMAS degradation of environmental barrier coatings,“ *Surface and Coatings Technology*, Bd. 202, pp. 653-657, 2007.
- [8] A. F. Renteria, „A small-angle scattering analysis of the influence of manufacture and thermal induced morphological chnages on the thermal conductivity of EB-PVD PYSZ thermal barrier coatings,“ RWTH aachen, Mexico, 2006.
- [9] U. Leushake, T. Krell, U. Schulz, M. Peters, W. A. Kaysser, B.H. Rabin, „Microstructure and phase stability of EB-PVD alumina and alumina/zirconia for thermal barrier coating applications,“ *Surface and Coating Technology*, Bd. 94, pp. 131-136, 1997.
- [10] L. Wang, D.C. Li, J.S. Yang, F. Shao, X. H. Zhong, „Modeling of thermal properties and failure of thermal barrier coatings with the use of finite element methods,“ *Journal of European Ceramic Society*, Bd. 36, pp. 1313-133, 2016.
- [11] T.Krell, U. Schulz, M. Peters, W. A. Kaysser, „EB-PVD Zirconia thermal barrier coatings with graded Alumina-PYSZ interlayers,“ pp. 197-204, 2001.
- [12] U. Schulz, M. Peters, Fr.W. Bach, G. Tegeder, „Graded coating for thermal, wear and corrosion barriers,“ *Materials Science and Engineering*, Bd. A 362, pp. 61-80, 2003.
- [13] S. Bose, „Plasma Sprayed and EB PVD TBCs,“ in *High Temperature Coatings*, 2007, pp. 162-224.

- [14] Tom Strangman, Derek Raybould, Ahsan Jameel, Wil B, „Damage mechanisms, life prediction and development of EB-PVD thermal barrier coating for turbine airfoils,“ *Surface and coating technology*, Bd. 202, pp. 658-664, 2007.
- [15] R. Naraparju, U. Schulz, P. Mechnich, P. Döbber, F. Seidel, „Degradation study of 7 wt% yttria stabilized zirconia (7YSZ) thermal barrier coatings on aero-engine combustion chamber parts due to infiltration by different CaO-MgO- Al<sub>2</sub>O<sub>3</sub>-SiO<sub>2</sub> variants,“ *Surface and Coatings Technology*, Bd. 260, pp. 73-81, 2014.
- [16] S. Bose, „High Temperature Coatings,“ 2007, pp. 155-168.
- [17] R. Reed, *The Superalloys Fundamentals and Applications*, New York: Cambridge university press, 2006.
- [18] Peter Mechnich, Wolfgang Braue, Uwe Schulz, „High-Temperature corrosion for EB-PVD yttria partially stabilized zirconia thermal barrier coatings with an artificial volcanic ash overlay,“ *Journal of American Ceramic Society*, Bd. 94[3], pp. 925-931, 2011.
- [19] U. Schulz, K. Fritscher, C. Leyens, M. Peters, „High Temperature Aging of EB-PVD Thermal barrier Coatings,“ in *International Conference on Advance Ceramics and Structures*, Cocoa Beach, Florida, 2001.
- [20] U. Leushake, T. Krell, U. Schulz, M. Peters, W.A. Laysser, B.H. Rabin, „Microstructure and phase stability of EB-PVD alumina and alumina/zirconia for thermal barrier coating applications,“ *Surface and Coating Technology*, Bd. 94, pp. 131-136, 1997.
- [21] Martin Frommherz, Alfred Scholz, Matthias Oechsner, „Gadolinium zirconate/YSZ thermal barrier coatings: Mixed-mode interfacial fracture toughness and sintering behavior,“ *Surface & Coatings Technology*, Bd. 286, p. 119–128, 2016.
- [22] C. Bharat, „Thermal Barrier coatings,“ Kota, 2006.
- [23] Mohammadreza Daroonparvar, Muhamad Azizi Mat Yajid, „Improvement of thermally grown oxide layer in thermal barrier coating system with nano alumina as third layer,“ *Transactions of Nonferrous Metals Society of China*, Bd. 23, pp. 1322-1333, 2013.
- [24] A.M. Karlsson, J.W. Hutchinson, A.G. Evans, „The displacement of the thermally grown oxide in thermal barrier coating system upon temperature cycling,“ *Materials Science and Engineering*, Bd. A351, pp. 244-257, 2003.
- [25] T.M. Pollock, D.M. Lipkin, and K.J. Hemker, „Multifunctional coating interlayers for thermal barrier systems,“ *Materials Research Society*, Bd. 37, pp. 923-931, 2012.
- [26] W. Walston, „Coating And Surface Technologies For Turbine Airfoils,“ *The Minerals, Metals and Material Society*, pp. 579-583, 2004.

- [27] Ramesh Agarwal, Melih Cemal Kushan, Sinem Cevik Uzgur, Yagiz Uzunonut and Fehmi Diltemiz , Recent Advances in Aircraft Technology, Croatia: InTech, 2012.
- [28] V. Postolenko, „Failure mechanisms of thermal barrier coatings for high temperature gas turbine components under cyclic loading,“ RWTH Aachen, Aachen, 2008.
- [29] Khamirl Amin Matori, Loy Chee Wah, Mansor Hashim, Ismayadi Ismail, Mohd Hafiz Mohd Zaid, „Phase Transformations of  $\alpha$ -Alumina Made from waste aluminum via a precipitation technique,“ *International Journal of Molecular Sciences*, Bd. 13, pp. 16812-16821, 2012.
- [30] Merlin G.J. Müller, Farwah Nahif, Joachim Mayer, Jochen M. Schneider, „Transmission electron microscopy investigation of the effect of Si alloying on the thermal stability of amorphous alumina thin films deposited by filtered cathodic arc deposition,“ *Surface and Coating Technology*, Bd. 257, pp. 338-347, 2014.
- [31] Leva Zake-Tiluga, Visvaldis Svinka, Ruta Svinka, Bodo Zierath, Peter Greil, Tobias Fey, „Thermal conductivity and microstructure characterisation of lightweight alumina and alumina-mullite ceramics,“ *Journal of European Ceramic Society*, Bd. 36, pp. 1469-1477, 2016.
- [32] Maria Iaponeide Fernandes Macedo, Celso Aparecido Bertran, Carla Cristiane Osawa, „Kinetics of the  $\gamma \rightarrow \alpha$ -alumina phase transformation by quantitative X-ray diffraction,“ *Journal of Material Science*, Bd. 42, pp. 2830-2836, 2007.
- [33] A. A. Mohsin, „Residual Stress and Fracture in High Temperature Ceramics,“ The University of Manchester, 2012.
- [34] F. Nahif, S. Mraz, D. Music, P. Keuter, J.M. Schneider, „Ab initio and experimental study on the effect of Y additions on the phase formation and thermal stability of Al<sub>2</sub>O<sub>3</sub> thin films deposited by filtered cathodic arc evaporation,“ *Surface and Coating Technology*, Bd. 257, pp. 333-337, 2014.
- [35] A. Keyvani, M. Saremi, M. Heydarzadeh Sohi, „Microstructural stability of zirconia–alumina composite coatings during hot corrosion test at 1050°C,“ Bd. 506, pp. 103-108, 2010.
- [36] U.Leushake, T.Krell, U.Schulz, M.Peters, W.A.Laysser, B.H. Rabin, „Microstructure and phase stability of EB-PVD alumina and alumina/zirconia for thermal barrier coating applications,“ *Surface and Coating Technology*, Bd. 94, pp. 131-136, 1997.
- [37] Zhang Xiao-feng, Jin-bing, Min liu, „In situ synthesis of alpha alumina layer on the thermal barrier coating for protection against CMAS (CaO-MgO-Al<sub>2</sub>O<sub>3</sub>-SiO<sub>2</sub>) corrosion.,“ *Surface and Coating Technology*, Bd. 261, pp. 54-59, 2015.
- [38] A. Keyvani, M. Saremi, M. Heydarzadeh Sohi, „Microstrutural stability of zirconia-alumina composite coatings during hot corrosion test at 1050°C,“ *Journal of Alloys and Compounds*, Bd. 506, pp. 103-108, 2010.
- [39] P. Mohan, B.Yao, T. Patterson, Y.H. Sohn, „Electrophoretically deposited alumina as protective

- overlay for thermal barrier coatings against CMAS degradation," *Surface and Coating technology*, Bd. 204, pp. 797-801, 2009.
- [40] U. Schulz, T. Krell, U. Leushake, M. Peters, „Graded Design of EB-PVD Thermal Barrier Coating Systems," in *Agard Workshop on Thermal Barrier Coatings*, Aalborg, 1997.
- [41] R. Wellma, G. Whitman, J.R. Nicholls, „CMAS corrosion of EB PVD TBCs: Identifying the Minimum Level to Initiate Damage," *International Journal of Refractory Metals and Hard Materials*, Bd. 28, Nr. 1, pp. 124-132, 2009.
- [42] Carlos G. Levi, John W. Hutchinson, Marie-Herlene Vidal Setif, Curtis A. Johnson, „Environmental degradation of thermal barrier coatings by molten deposits," *Materials Research Society*, Bd. 37, pp. 932-941, 2012.
- [43] Aysegul Augun, Alexander L. Vasiliev, Nitin P. Padture, Xinqing Ma, „Novel thermal barrier coatings that are resistant to high temperature attack by glassy deposits," *Acta Materialia*, Bd. 55, pp. 6734-6745, 2007.
- [44] Ravisankar Naraparaju, Peter Mechnich, Uwe Schulz, Guillermo Cesar Mondragon Rodriguez, „The accelerating effect of calcium sulphate within CMAS and its effect on the infiltration behavior in EB-PVD 7YSZ," *Journal of American Ceramic Society*, pp. 1-6, 2015.
- [45] Wenshuai Li, Huayu Zhao, Xinghua Zhong, Liang Wang, and Shunyan Tao, „Air plasma-sprayed yttria and yttria stabilized zirconia thermal barrier coatings subjected to calcium-magnesium-alumino-silicate (CMAS)," Bd. 23 (6), pp. 975-983, 2014.
- [46] C. Mercer, S. Faulhaber, A. G. Evans and R. Dariola, „A delamination mechanism for thermal barrier coatings subject to calcium-magnesium-alumino-silicate (CMAS) infiltration.," *Acta Materialia*, Bd. 53, pp. 1029-1039, 2005.
- [47] A. K. Rai, R. S. Bhattacharya, „CMAS-Resistant Thermal Barrier Coatings (TBC)," *International Journal of Applied Ceramic Technology*, Bd. 7, pp. 662-674, 2010.
- [48] Uwe Schulz, Wolfgang Braue, „Degradation of La<sub>2</sub>Zr<sub>2</sub>O<sub>7</sub> and other novel EB-PVD thermal barrier coatings by CMAS (CaO–MgO–Al<sub>2</sub>O<sub>3</sub>–SiO<sub>2</sub>) and volcanic ash deposits," *Surface and Coating Technology*, Bd. 235, pp. 165-173, 2013.
- [49] Jiao-Jie Cui, Jia-Hu Ouyang, Zhan-Guo Liu, „Hot corrosion behaviour of Lanthanide magnesium hexaaluminate ceramic coated with molten CMAS deposits at temperature of 1250C in air," *Journal of Alloys and Compounds*, Bd. 685, pp. 316-321, 2016.
- [50] P. Mechnich, W. Braue, „Volcanic Ash-Induced Decomposition of EB-PVD Gd<sub>2</sub>Zr<sub>2</sub>O<sub>7</sub> Thermal Barrier Coatings to Gd-Oxyapatite, Zircon, and Gd, Fe-Zirconolite," *Journal of American Ceramic Society*, Bd. 96(6), pp. 1958-1965, 2013.
- [51] Ramanathan Krishnamurthy, David J. Srolovitz, „Sintering and microstructure evolution in columnar

- thermal barrier coatings," *Acta Materialia*, Bd. 57, pp. 1035-1048, 2009.
- [52] Vanni Lughì, Vladimir K. Tolpygo, David R. Clarke, „Microstructural aspects of the sintering of thermal barrier coatings," *Materials Science and Engineering*, Bd. A368, pp. 212-221, 2004.
- [53] Peter Mechnich, Wolfgang Braun, Hartmut schneider, „Multifunctional reaction-bonded alumina coatings for porous continuous fiber reinforced oxide composites," *International Journal of Applied Ceramic Technology*, Bd. 1[4], pp. 343-350, 2004.
- [54] U.Schulz, K. Fritscher, C. Leyens, M. Peters, „High Temperature Aging of EB-PVD Thermal barrier Coatings," in *International Conference on Advance Ceramics and Structures*, Cocoa Beach, Florida, 2001.
- [55] Krämer, Stephan; Yang, James; Levi, Carlos G., „Infiltration-inhibiting reaction of gadolinium zirconate thermal barrier coatings with CMAS melts," *Journal of the american ceramic society*, Bd. 91, Nr. 2, pp. 576-583, 2008.
- [56] Stephan Krämer, Yang James, Levi Carlos G, Johnson Curtis A, „Thermochemical interaction of thermal barrier coatings with molten CaO-MgO-Al<sub>2</sub>O<sub>3</sub>-SiO<sub>2</sub> (CMAS) deposits," *Journal of the American Ceramic Society*, Bd. 89, Nr. 10, pp. 3167-3175, 2006.
- [57] Wenjia Song, Kai-Uwe Hess, David E. Damby, Fabian B. Wadsworth, Yan Lavallee, Corrado Cimarelli, Donald B. Dingwell, „Fusion characteristics of volcanic ash relevant to aviation hazards," pp. 1-8, 2014.
- [58] Khalil Bouzazi, Habib Boughzala, Hmida Zamali, „Cation miscibility in KNO<sub>3</sub>eRbNO<sub>3</sub> binary system. A combined SEM,EDX and XRD Reitveld analysis," *Journal of Alloys and Compounds*, Bd. 680, pp. 512-521, 2016.
- [59] Takashi Shirai, Hideo Watanabe, Masayoshi Fuji, Minoru Takahashi, „Structural properties and surface charecteristics on alumina oxide powders," Ceramics Research Center, Gifu, Japan, 2009.
- [60] A. M. Abbas, „Residual Stress and Fracture in High Temperature Ceramics," The University of Manchester, 2012.
- [61] U. Leushake, T. Krell, U. Schulz, M. Peters, W. A. Kaysser, B.H. Rabin, „Microstructure and phase stability of EB-PVD alumina and alumina/zirconia for thermal barrier coating applications," *Surface and Coating Technology*, Bd. 94, pp. 131-136, 1997.
- [62] Amarendra Rai, Rabi Bhattacharya, Douglas Wolfe, Timothy Eden, „CMAS-reseistant thermal barrier coatings," *Internation Journal of Applied Ceramic Technology* , Bd. 7 (5), pp. 662-674, 2010.
- [63] Amanda R. Krause, Xing Li, Nitin P. Pature, „Interaction between ceramic powder and molten calcia-magnesia-alumino-silicate (CMAS) glass, and its implication on CMAS-resistant thermal barrier coatings," *Scripta Materialia*, Bd. 112, pp. 118-122, 2016.

